npj | imaging

Article

https://doi.org/10.1038/s44303-025-00093-z

Automated smartphone based cell analysis platform

Meryem Beyza Avci[1,2,3], Fatma Kurul[1], Mehmet Turkan[2] & Arif E. Cetin[1,4]

Cell analysis technologies play a critical role in biomedical research, enabling precise evaluation of essential parameters such as cell viability, density, and confluency. In this article, we introduce Quantella, a smartphone-based platform designed to perform comprehensive cell analysis encompassing these key metrics. Addressing limitations of conventional systems, such as high cost, hardware complexity, and limited adaptability, Quantella integrates low-cost optics, a rinsable flow cell, bluetooth-enabled hardware control, and a cloud-connected mobile application. Its adaptive image-processing pipeline employs multi-exposure fusion, thresholding, and morphological filtering for accurate, morphology-independent segmentation without requiring deep learning or user-defined parameters. System validation studies across diverse cell types showed deviations under 5% from flow cytometry. With the capacity to analyze over 10,000 cells per test, Quantella delivers high-throughput, reproducible results. Its accessible, scalable design makes it a promising tool for biomedical research, diagnostics, and education, particularly in resource-limited settings.

Accurate cell analysis is the cornerstone of modern biological research, underpinning discoveries from drug development to regenerative medicine. Cell analysis encompasses various parameters, including cell viability, density, and confluency, each essential for understanding cell health, growth, and behavior[1,2]. Viability assessment enables researchers to distinguish live cells from dead ones, providing critical insights into culture health. Cell density measurement provides an accurate count of cells within a sample, ensuring consistency across experiments and supporting reproducible results in studies that rely on precise cell quantities. Confluency analysis gauges the surface area covered by cells, a valuable metric in studies where uniform cell coverage is crucial, such as drug screening and proliferation studies. Traditionally, cell analysis has relied on manual techniques, such as hemocytometers for assessing cell density and viability, and visual estimation for confluency[3,4]. While hemocytometers have been widely used in laboratories due to their low cost, manual counting is time-consuming and can lead to inconsistent results. Automated systems, however, use imaging, electrical impedance, spectrophotometry, absorbance/fluorescence measurement, and flow cytometry, which are enhanced with advanced algorithms, to measure cell viability and density with greater precision and reproducibility[5,6]. On the other hand, for confluency analysis, recent advancements in imaging software now enable automated systems, e.g., relying on brightfield microscopy, to quantify confluency based on pixel density and pattern recognition algorithms, providing consistent, objective measurements that support high-throughput applications[7–9].

Automated cell analysis technologies have emerged with unique strengths suited to diverse applications and budget considerations, enabling researchers to choose based on their specific needs for throughput, accuracy, and resolution. For instance, flow cytometry offers high sensitivity and can perform complex multiparametric analyses by using fluorescence and laser-based systems[10]. The technology is well-suited for applications requiring detailed cellular profiles, such as immunophenotyping and viability assessment, while the cost and technical expertise can be prohibitive, limiting its use in research settings. Electrical impedance-based cytometry measures changes in electrical properties as cells pass through an electric field, providing a label-free approach for real-time viability and density monitoring[11]. This technology excels in noninvasive applications and is particularly useful for proliferation studies; however, its complexity and cost may limit its accessibility, especially in smaller labs. Spectrophotometry and plate-based fluorescence readers, meanwhile, focus on bulk cell measurements and are widely used for high-throughput viability assays, making them efficient for large sample sets[12]. However, these systems lack the single-cell resolution of other technologies and are less suitable for applications needing morphological detail. Among these, image-based cytometry stands out for its adaptability to low-cost implementations, making it an attractive option for laboratories needing basic cell analysis without high infrastructure costs, while other technologies serve more specialized roles where detail, speed, and throughput are prioritized. By leveraging digital imaging with straightforward stains, e.g., trypan blue[13], image-based systems allow

[1]Izmir Biomedicine and Genome Center, Izmir, Turkey. [2]Department of Electrical and Electronics Engineering, Izmir University of Economics, Izmir, Turkey. [3]Izmir International Biomedicine and Genome Institute, Dokuz Eylul University, Izmir, Turkey. [4]Department of Biophysics, Faculty of Medicine, Dokuz Eylul University, Izmir, Turkey. e-mail: arifengin.cetin@ibg.edu.tr

laboratories to achieve consistent results without the higher costs associated with specialized equipment, making it an accessible choice for routine applications. Automated confluency analysis systems, relying on image-based methodology, leverage a variety of advanced data processing techniques, including imaging-based algorithms[14], machine learning models[15], phase contrast detection[16], fluorescence image analysis[17], and optical density measurements[18]. These technologies process raw data from images or signals to determine the proportion of a surface covered by cells, often without requiring labels or manual intervention. By integrating edge detection, segmentation algorithms, and pattern recognition methods, such systems ensure precise and reproducible quantification of cell confluency across diverse cell types and experimental conditions. Additionally, some platforms incorporate real-time data analysis and adaptive models to accommodate variations in cell morphology and growth patterns, enhancing the reliability of confluency measurements over time.

Building on the strengths of imaging-based cytometry, we have developed Quantella, a cell analysis platform capable of performing three critical analyses, e.g., cell viability, cell density, and confluency, on a single platform. Quantella employs a smartphone-integrated low-cost optical system capable of imaging individual cells as small as 5 μm, enabling high-resolution and high-throughput analysis. The optofluidic platform, featuring a built-in pump system, automates sample delivery and enables self-cleaning of the microfluidic compartment, ensuring consistent performance and streamlined workflows. Quantella's rinsable flow cell enhances its versatility by offering both single- and multi-use options, supported by a validated cleaning protocol. This feature provides a practical solution for a wide range of research needs, e.g., sterile applications requiring strict contamination control or cost-effective high-throughput experiments. Quantella achieves accurate cell identification and distinction without relying on sophisticated hardware or requiring extensive training with large datasets as demanded by deep learning-based systems, thanks to its novel image-processing algorithm. This novel image-processing algorithm includes an initial image enhancement step that improves the quality of raw data, allowing for higher accuracy in cell segmentation. By enhancing raw images, the algorithm ensures clearer boundaries and better contrast, significantly boosting the reliability of cell detection and analysis. Unlike traditional morphology-dependent methods, this adaptive algorithm is not cell-specific and does not require user-defined parameters, making it highly versatile across various cell types. The algorithm uses multi-weight-map analysis to deliver superior segmentation, even for densely clustered adherent cells, eliminating the need for complex suspension procedures. By using large sample sizes, e.g., >10,000 cells per test, Quantella ensures low error rates and enhances statistical reliability, particularly when compared to approaches relying on relatively smaller sample sizes, which often lead to higher variability and inaccuracies. Hence, our approach achieves deviations of less than 5% compared to flow cytometry, the gold standard for cell analysis, underscoring its precision and robustness. We have rigorously validated on a diverse range of cell types, including suspension and adherent cell lines, as well as primary cells, e.g., red blood cells (RBCs), where we evaluated 12 representative cell types, achieving over 90% accuracy in cell identification and discrimination. Quantella integrates Qtouch, a custom-designed smartphone application that offers intuitive control over hardware functions, such as camera and pump operations. Qtouch facilitates image processing and analysis, enabling researchers to measure cell viability, density, and confluency within the same smartphone application. By automating these processes and minimizing user intervention or reliance on user-driven parameters, the system ensures reliable and efficient cell analysis at every step, eliminating the need for experienced users. Quantella combines advanced imaging, adaptive algorithms, and automated liquid handling in a compact and affordable system. By offering an all-in-one solution for cell viability, density, and confluency analysis, it serves as an accessible, efficient, and reliable tool, setting a new standard for scientific and clinical cell analysis applications.

Results

Hardware components of Quantella

Figure 1A displays the schematic illustration and the photograph of Quantella, respectively. For hardware control and data acquisition/management, we used a 2019 Model Oppo Reno 10× Zoom. The platform incorporates an Arducam lens (f≈16 mm) positioned in front of the smartphone camera lens to enhance imaging capability. Sample illumination is provided by a white light-emitting diode (LED) source, and a manual linear stage is integrated to adjust focus as needed. The microcontroller and LED light source are powered by a 3.7 V lithium-ion polymer (LiPo) battery, rechargeable via an integrated charging unit. An amplifier increases the voltage to 12 V to support the microcontroller. A bluetooth unit enables the control of the pump through Quantella's smartphone application, facilitating seamless operation and user interaction. Quantella integrates a smartphone application, Qtouch (Fig. 1B), with a cloud server to enable automated and efficient cell analysis. Qtouch facilitates image capture, experiment management, and hardware control via bluetooth, while the cloud server employs image-processing algorithms to perform cell counting, viability, and confluency analysis. Processed results, including labeled images and quantitative data, are transmitted back to the application for real-time visualization, providing researchers with a user-friendly, adaptable, and efficient workflow suitable for diverse experimental setups.

Figure 1C demonstrates Quantella's imaging capabilities in assessing cell viability and confluency in single-cell resolution. In the cell density-viability analysis panel (left) of Qtouch, CHO DG44 cells stained with trypan blue are differentiated by Quantella, with live cells encircled in green and dead cells encircled in red, as indicated by the arrow. In the confluency analysis panel (right), high-contrast imaging captures the detailed morphology and distribution of MCF-7 cell clusters highlighted with green, enabling accurate confluency measurements. Figure 1D demonstrates Quantella's imaging capability, resolving Group 9, Element 3 on the USAF 1951 resolution test chart, which corresponds to a feature size of ~0.775 μm. As this group represents the finest feature available on this chart, Quantella achieves a minimum resolution of 1.55 μm. This result highlights Quantella's high-resolution capability within the limits of the current test chart, confirming its reliability for applications that require precise imaging of cells and samples. Figure 1E shows images of a wide range of specimens captured by Quantella, demonstrating its versatility and capability to deliver high-resolution images across various biological scales. Quantella's high-resolution imaging capability, with a field-of-view (FOV) of 3.2 mm × 4.2 mm, enables imaging tissue samples in single-cell resolution, such as the cervix uteri (left). Its detailed imaging allows for the visualization of individual cells as small as 5 μm, such as L929 cells (middle) or RBC (right). The large FOV imaging capability also allows Quantella to accommodate larger specimens, such as zebrafish larvae (see "Methods" section for details of the cell culture protocols).

Sample delivery is managed by a piezoelectric pump (Bartels Mikrotechnik GmbH), controlled by an Arduino microcontroller. As shown in Fig. 1F, the microcontroller adjusts the pump's flow rate by modulating the supply voltage (1.0–4.5 V) via pulse-width modulation (PWM) at 100 Hz. Flow rate calibration was performed using DI-water, with mass measurements taken over 60 s intervals at eight voltage levels. The results confirmed a linear relationship between voltage and flow rate. The optofluidic setup includes a single-channel flow cell for sample delivery. The channel width is set to 100 μm, similar to hemocytometer counting chambers, with dimensions of 50 mm × 8 mm. The flow cell is constructed with adhesive tape serving as an interlayer between two polymethyl methacrylate or acrylic sheets, defining the fluidic channel. The sample, consisting of a 1:1 mixture of trypan blue and cell suspension, was infused into the channel using the piezoelectric pump and subsequently directed to waste. To prevent motion artifacts, the piezoelectric pump was deactivated during image capture, and a brief pause was introduced to allow fluid motion to settle fully, ensuring that all images were acquired under static, no-flow conditions. After each test, the flow channel was cleaned with phosphate-buffered saline (PBS) and distilled water to maintain system integrity.

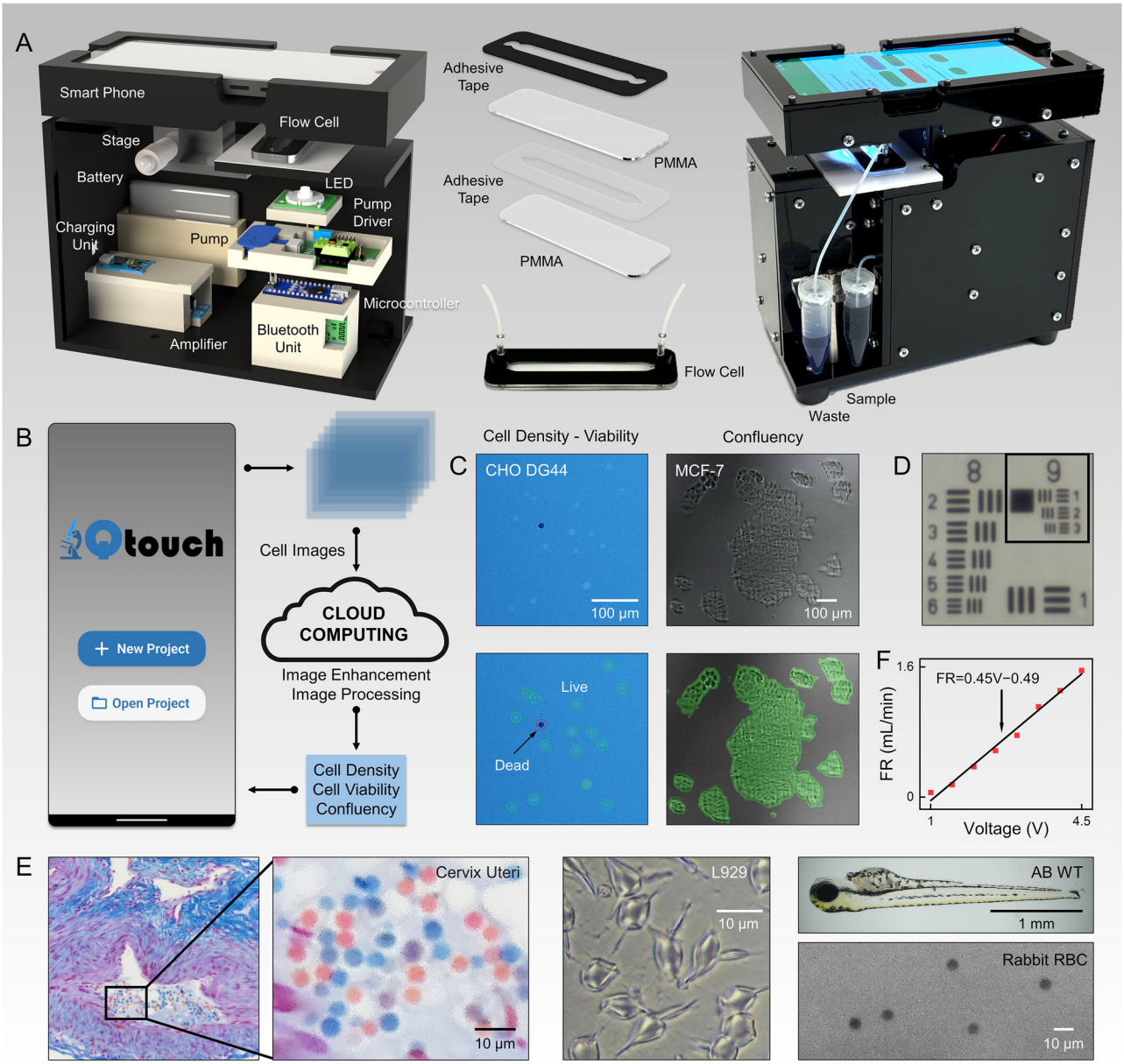

Fig. 1 | Hardware and software components of Quantella. A Schematic illustration and photograph of Quantella and the flow cell. Key labeled components include the smartphone (Oppo Reno 10× Zoom), external Arducam lens (~16 mm focal length), LED illumination source, microcontroller, LiPo battery, and flow cell. **B** The smartphone application, Qtouch, developed for hardware control and analyses of cell density, viability, and confluency. The image shows the density-viability analysis panel. **C** Left: Image of CHO DG44 cells in trypan blue solution, with processed results indicating live cells circled in green and dead cells circled in red. Right: Confluency analysis image, with processed areas showing segmented cells highlighted in green. **D** Image of the USAF 1951 resolution test chart captured by Quantella, resolving Group 9, Element 3 (feature size ~0.775 μm), indicating a minimum resolution of ~1.55 μm. **E** Images of a wide range of specimens, including cervix uteri tissue (zoomed in on cervical cells), L929 fibroblast-like cells, AB strain wild-type (AB WT) zebrafish, and rabbit RBCs. **F** Relationship between flow rate of the piezoelectric pump and the applied voltage (1.0–4.5 V). A linear regression model (black line) was fitted to the experimental data points (red dots), which represent the average values ($n = 5$).

Image enhancement for cell counting

Figure 2A illustrates the proposed image processing algorithm, which starts with an original 4000 × 3000 × 3 pixel image with 8 bits per pixel (Step I) converted to grayscale, I (Step II). For the dead cell detection task, the grayscale image is further inverted by subtracting its pixel values from 255 (i.e., digital negative) (Step III). To address nonuniform illumination conditions caused by the Gaussian distribution of the light source, the average background illumination is estimated with a sensitivity value of 0.5. This value was empirically determined based on performance optimization across a range of cell types and illumination conditions to ensure effective background correction without loss of cellular detail. This estimated background is then subtracted from the image to achieve uniform illumination (Step IV). Finally, a 2D Gaussian filter with a standard deviation (SD) of $\sigma = 1.2$ is applied to the image to reduce the noise and enhance the segmentation accuracy. These values were empirically determined to balance noise suppression with preservation of relevant morphological features. Since each cell possesses its unique characteristics, such as transparency and brightness, distinguishing cells and their boundaries in some images could be challenging. To address this issue, gamma transformation is applied using 11 different empirically determined gamma values ($\gamma_1 = 0.75$, 1.0, 1.25, 1.50, 1.75, 2.0, 2.25, 2.5, 2.75, 3.0, 4.0), aiming at enhancing the visibility of details across varying brightness levels. This range

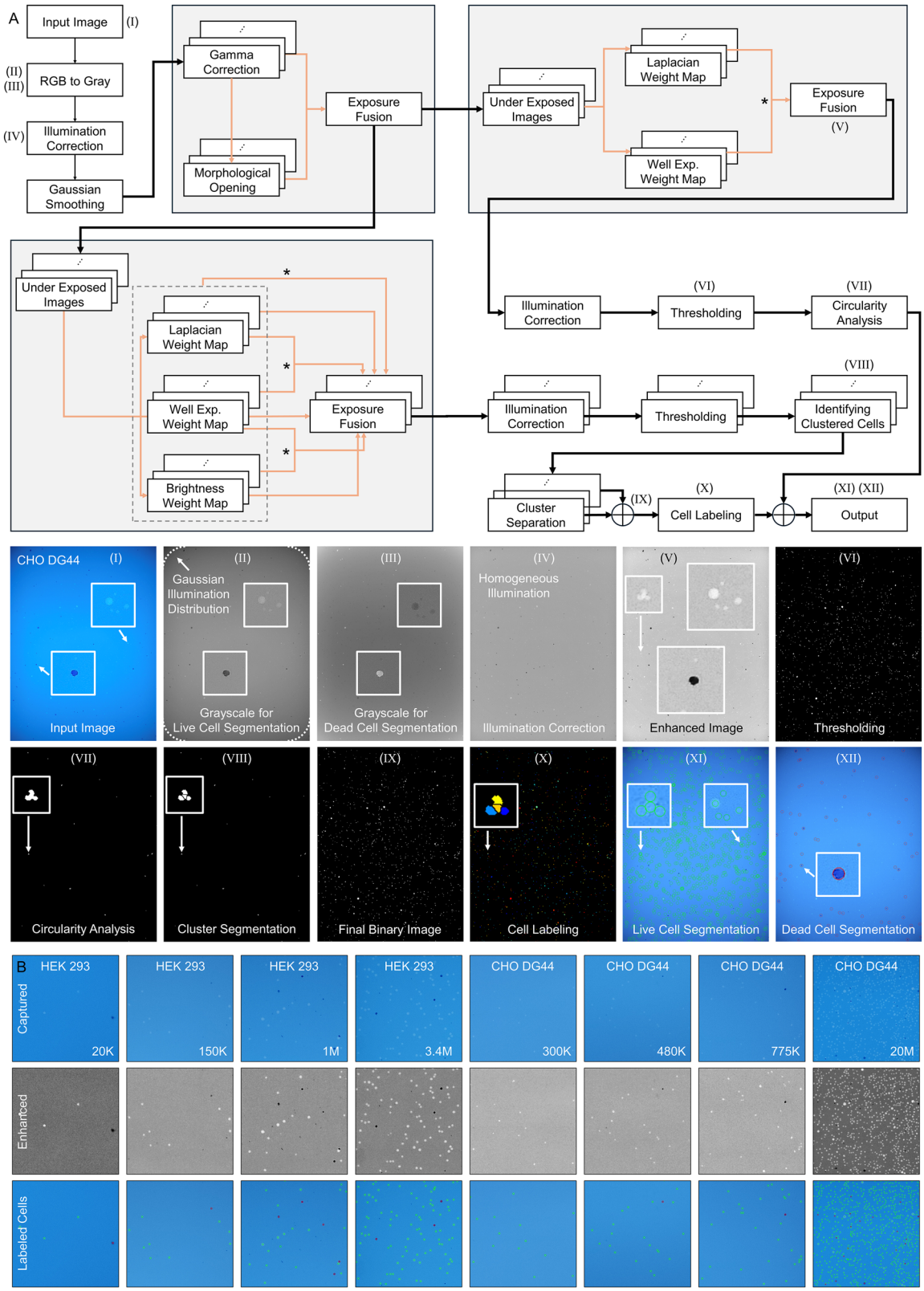

Fig. 2 | Image processing algorithm for cell counting feature of Quantella. **A** Flowchart illustrating the workflow of the image-processing algorithm for cell counting, e.g., cell viability and density, along with the processed images of a representative CHO DG44 cell sample at each processing step. **B** Cell counting results for HEK 293 and CHO DG44 cell samples with varying density levels, together with their initial and enhanced images.

was chosen to enhance contrast in both dim and overly bright regions, which in turn sharpened cell boundary visibility without causing saturation or detail loss. Through repeated testing across diverse imaging conditions and datasets, these gamma values consistently delivered the most reliable segmentation outcomes, and were therefore incorporated into the image-processing workflow to ensure robustness and reproducibility. As an additional note, gamma correction is influenced by factors such as sensor gain, native gamma encoding, and the characteristics of color filter arrays,

which can vary significantly across smartphone models. In our current implementation, Quantella is designed as a dependent hardware-software unit, in which both the smartphone and the image-processing code are co-optimized and fixed as part of the compact device. This ensures consistent imaging behavior and algorithmic performance, but it also means that the system, as presently constructed, is not directly portable across arbitrary Android or iOS devices. The tight coupling between the smartphone hardware and software was a deliberate design choice to ensure image stability, reproducibility, and control over processing variables.

Following gamma correction, an opening (morphological) operation with a disk kernel of radius 5 is applied to all gamma-adjusted images. This operation removes minor artifacts (e.g., debris) and smooths cell boundaries obscured by brightness and transparency variations, ensuring that only well-defined cell structures are retained for further analysis.

At this stage, a multi-scale image fusion method is employed to generate a single composite image. This approach starts by decomposing each gamma-transformed image into multiple levels using a Laplacian pyramid (**L**), which retains details across various spatial resolutions. Simultaneously, the corresponding fusion maps are processed through a Gaussian pyramid (**G**), ensuring smooth transitions between levels. For each pyramidal level *l*, the fusion process is expressed as:

$$\mathbf{L}\{F^l\} = \sum_{n=1}^{11} \mathbf{G}\{W_n^l\}\mathbf{L}\{I_n^l\} \tag{1}$$

where *Wn* represents the dedicated weight map derived from the output of the opening operation on I_n, and I_n represents the *n*th gamma-corrected image. This formula integrates gamma-transformed images with their respective weight maps across all levels of the pyramid, producing a fused Laplacian decomposition $\boldsymbol{L}\{F^l\}$. This fused decomposition captures both prominent and subtle details across varying brightness levels[19]. The fused pyramid $\mathbf{L}\{F^l\}$ is finally collapsed to obtain the output image I' (See Algorithm 1).

Algorithm 1. First Pass

Require: Grayscale input image I
Ensure: Enhanced output image I'
function EnhaceImageFirstPass(I)
  smoothed ← ApplyGaussianFilter(I, $\sigma = 1.2$)
  γ_1←[0.75, 1.0, 1.25, 1.5, 1.75, 2.0, 2.25, 2.5, 2.75, 3.0, 4.0]
  images ← ApplyGammaCorrection(smoothed, γ_1)
  structElem ← CreateDiskElement(5)
  weights ← ApplyMorphologicalOpening(images, structElem)
  fused ← PerformExposureFusion(images, weights)
  return I'
end function

The resulting image $I\prime$ from this exposure fusion operation is yet artificially underexposed using seven different empirically determined gamma values ($\gamma_2 = 1.75, 2.0, 2.25, 2.5, 2.75, 3.0, 4.0$). These gamma transformations further enhance the visibility of finer cell features by gradually darkening the overall image, making faint edges and internal structures more distinguishable in the final output.

Each underexposed image $I'_k, k = 1 \ldots 7$, is processed to generate distinct weight maps, e.g., Laplacian and Well-Exposedness. The Laplacian operation enhances the visibility of cell boundaries and other high-frequency details by assigning greater weights to regions with sharper edges and finer textures. To achieve this, a 3×3 simple Laplacian sharpening kernel is applied to each input image, resulting in the Laplacian weight map ($W_{L,k}$). In addition, the well-exposedness function prioritizes pixels that fall within the optimal brightness range, producing a well-exposedness weight map ($W_{E,k}$) that highlights regions with balanced brightness, e.g., neither overly dark nor excessively bright[20]. The well-exposedness weight map is expressed as:

$$\mathrm{W}_{E,k}(\mathrm{x},\mathrm{y}) = \exp\left(-\frac{\left(I'_k(x,y) - \left(1-\mu_k\right)\right)^2}{2\sigma_k^2}\right) \tag{2}$$

where I'_k is the *k*th underexposed image, μ_k is the mean intensity of I'_k, and σ_k is the SD of I'_k. These calculated weight maps are first normalized to the range [0, 1], and then combined through element-wise multiplication to generate final fusion maps W_k, i.e., $\{W_k\}_{k=1}^7 = \{W_{L,k} \bigotimes W_{E,k}\}_{k=1}^7$. As the final step, the enhanced image ($I\prime\prime$) is generated using the multi-scale pyramidal fusion method outlined and detailed above (Step V). This multi-level enhancement highlights cells across all intensity levels, significantly improving counting accuracy in the algorithm (see Algorithm 2).

Algorithm 2. Second Pass

Require: Enhanced image from the first pass I'
Ensure: Further enhanced output image I''
function EnhaceImageSecondPass(I')
  γ_2←[1.75, 2.0, 2.25, 2.5, 2.75, 3.0, 4.0]
  I_k ← ApplyGammaCorrection(I', γ_2)
  Initialize $W_{L,k}$, $W_{E,k}$
  for each $\gamma_i \in \gamma_2$ **do**
    $W_{L,k}[\gamma_i]$ ←ComputeLaplacianWeight($I\gamma_i$)
    $W_{E,k}[\gamma_i]$ ←ComputeWellExposednessWeight($I\gamma_i$)
  end for
  $W_k \leftarrow W_{L,k} \cdot W_{E,k}$
  I'' ← PerformExposureFusion(I_k, W_k)
  return I''
end function

Thresholding and circularity analysis

To create a binary segmentation mask, the histogram of the input image ($I\prime\prime$) is calculated to analyze the statistical distribution of pixel intensities. The peak intensity of this distribution is identified using the Gaussian fit. Starting from this peak, the first intensity level at which the Gaussian fit drops below a specified frequency threshold of 1000 is determined, as it marks the transition to low-intensity regions where cells are no longer present. This intensity level is used as the segmentation threshold, and a binary image is produced based on this threshold. In other words, pixels with intensities exceeding the identified level are marked as 1 (true), else as 0 (false), in the binary image. In order to smooth object edges and remove imperfections, a binary opening operation is applied using a disk-shaped structuring element with a radius of 2. As a final step, a border mask with a width of 1 is employed to remove potential artifacts near image borders, and it is then subtracted from the morphologically processed binary image to obtain the segmented image (I''_b) (Step VI). Circularity (C) is utilized to distinguish between single cells and clustered cells, which is calculated via Rosenfeld formula, relating an object's area (A) to its perimeter (P), quantifying how closely the object's shape approximates that of a perfect circle, $C = 4\pi \times A/P^2$ [21]. Following the circularity analysis, the regions with low circularity (<80%) are identified in the binary image I''_b. The regions representing only single cells are then used to form a new image $I''_{singlets}$ and the regions with clustered cells to form another new image $I''_{clusters}$. The watershed algorithm is then applied to clustered regions, which further enables the segmentation procedure to separate individual cells within these clusters (Step VII).

Cluster segmentation

Cluster segmentation is performed to differentiate aggregated cells by employing multiple weight maps, including Laplacian, well-exposedness, brightness, and their combinations, to emphasize distinct features within each cluster. In this process, the resulting image I' from the first pyramidal fusion operation is underexposed using the same γ_2 values. Laplacian ($W'_{L,k}$) and well-exposedness ($W'_{E,k}$) weight maps of these underexposed images are extracted as described previously. In addition, the brightness feature, a factor

influenced by saturation, plays a crucial role in improving the clarity of cell boundaries. To enhance the distinction of clustered cells, brightness-weight maps are employed to emphasize regions with significant intensity variation and to improve the overall visibility of cells within clusters.

First, the mean intensity (μ'_k) across all pixels in I'_k is calculated, and the initial brightness map $W'_{B,k}$ is obtained through the absolute deviation of each pixel intensity from the mean, e.g., $W'_{B,k} = |I'_k - \mu'_k|$[22]. To highlight not sufficiently saturated pixels more, the computed brightness maps are enhanced via histogram equalization. In detail, brightness histograms are computed to calculate an approximate probability mass function, and the denormalized and inverted cumulative mass function is applied as the transfer function for histogram-based enhancement. This step aids in adjusting the image to improve contrast, emphasize areas with significant brightness variation, and enhance the visibility of cell boundaries and structures. Finally, the calculated weight maps are first normalized to the range [0, 1] and then combined with element-wise multiplication, e.g., $\{W'_{LE,k}\}_{k=1}^{7} = \{W'_{L,k} \bigotimes W'_{E,k}\}_{k=1}^{7}$, $\{W'_{LB,k}\}_{k=1}^{7} = \{W'_{L,k} \bigotimes W'_{B,k}\}_{k=1}^{7}$ and $\{W'_{EB,k}\}_{k=1}^{7} = \{W'_{E,k} \bigotimes W'_{B,k}\}_{k=1}^{7}$. From this multiplication, 6 different weight maps per image I'_k are obtained, e.g., $W'_{L,k}$, $W'_{E,k}$, $W'_{B,k}$, $W'_{LE,k}$, $W'_{LB,k}$ $W'_{EB,k}$.

These maps are then utilized in another multi-scale pyramidal fusion process together with underexposed images (I'_k). Hence, this step generates six different fused outputs, each corresponding to one of the six weight maps, which highlight differently featured details in the underexposed images. To further address the nonuniform intensity distribution in these six fused images, illumination correction is once more applied, followed by thresholding to convert them into binary, as described above. After thresholding, clustered cell locations are fetched from the $I''_{clusters}$ image (Step VII), and only these cluster regions are processed by automatically tailoring specific binary masks for each image. This selective masking restricts further processing only to the identified clustered regions, ensuring computational efficiency. A circularity analysis is then performed on each cluster across all six images. For each cluster, the image with the lowest circularity value (<80%) is selected, as it most accurately represents aggregated cells. This approach ensures that regions of low circularity, indicative of cell clusters, are prioritized, while higher circularity regions, which might incorrectly represent clusters as single cells, are disregarded. The selected image is then used to segment the respective cluster into single cells using the watershed segmentation algorithm (Step VIII). In the final step, all segmented clusters are merged into a single output image ($I''_{segmented}$) and combined with $I''_{singlets}$ using a union operation to produce the final segmented image, e.g., $I_{final} = I''_{singlets} \bigcup I''_{segmented}$ (Step IX) (See Algorithm 3).

Algorithm 3. Cluster Segmentation

Require: Input image (I'), labeled clusters (*clusterLabels*), number of clusters (*numClusters*)

Ensure: Final segmented mask (I_{final})

function SegmentClusters(I', *clusterLabels*, *numClusters*)
  weightMaps[$W'_{L,k}$, $W'_{E,k}$, $W'_{B,k}$, $W'_{LE,k}$, $W'_{LB,k}$ $W'_{EB,k}$] ← GenerateWeightMaps(I')
  I_{final} ← Initialize empty mask
  for *clusterID* ← 1 **to** *numClusters* **do**
    lowestCircularity ← 0.8, *bestMap* ← 0
    for *mapID* ← 1 **to** N **do**
      $I''_{clusters}$ ← Threshold(weightMaps[*mapID*]) ∧ (*clusterLabels* == *clusterID*)
      if IsEmpty($I''_{clusters}$) **then** $I''_{clusters}$←(*clusterLabels* == *clusterID*)
      end if
      if CheckCircularity($I''_{clusters}$) <lowestCircularity **then**
        lowestCircularity ← CheckCircularity($I''_{clusters}$), *bestMap*←*mapID*
      end if
    end for
    $I''_{segmented}$ ← Watershed(weightMaps[*bestMap*])
    I_{final} ←$I''_{singlets}$ ∨$I''_{segmented}$
  end for
  return I_{final}
end function

Cell counting

Area thresholding is applied during dead cell detection to exclude debris resulting from Trypan Blue staining. To visualize the detected cells, regions from I_{final} are labeled using 8-connected components analysis (Step X). The labeled cells are overlaid onto the RGB input image, with centroids marked in green for live cells (Step XI) and red for dead cells (Step XII). Additionally, the live and dead cell counts for the selected image are displayed to the user. The camera FOV screens a volume of 1.344 µL on the flow cell. Cell concentration, representing the number of live cells/mL, is calculated by multiplying the live cell count by the dilution factor (due to trypan blue staining, e.g., 2) and dividing by the chamber volume monitored by the camera. Finally, cell viability (in percentage) is calculated by dividing the live cell count by the total cell count. Figure 2B shows the cell counting results for HEK 293 and CHO DG44 cell samples with varying density levels, together with their initial and enhanced images, which demonstrate the computational capability of our algorithm.

Performance study

To assess the performance of the algorithm, live and dead cells in images captured by Quantella are manually counted, establishing a baseline for an objective comparison. Confusion matrices are then generated by means of correct and incorrect counts to evaluate key performance parameters. In this specific context, confusion matrices are based on the following definitions: True Positives (TP) represent the cells correctly identified as live or dead by the algorithm. Figure 3A shows that Qtouch successfully identifies (i) five live SNU-449 cells and (ii) one dead HEK 293 cell in the input images. False Positives (FP) occur when the algorithm incorrectly identifies non-cell regions as cells. Figure 3A shows that Qtouch (iii) mistakenly identifies an extra cell in a cluster of three HEK 293 cells, resulting in a total of four detected cells, and (iv) incorrectly identifies a debris particle as a dead MCF-7 cell. False Negatives (FN) are the cells that the algorithm fails to detect, which are likely live or dead based on manual review. Figure 3A shows that Qtouch missed (v) one live HEK 293 cell and (vi) one dead HEK 293 cell in the images. True Negatives (TN) are marked as not applicable in this context, as they represent regions correctly identified as empty by the algorithm, but their infinite number of potential locations make practical quantification unfeasible. After identifying TP, FP, and FN values, three performance metrics, e.g., precision, recall, and F1-score, are calculated to evaluate the accuracy and reliability of the proposed algorithm in cell detection and counting.

Precision (P) measures the algorithm's accuracy in cell identification, specifically assessing the proportion of correctly identified cells (TP) among all cells labeled by the algorithm (sum of TP and FP), e.g., $P = TP/(TP + FP)$. A higher precision score indicates fewer FP's, meaning the algorithm is less likely to mislabel empty regions or artifacts as cells. Recall (R) measures the algorithm's sensitivity, indicating the proportion of actual cells in the sample that are correctly detected (TP). It is calculated as the ratio of TP to all actual cells (sum of TP and FN), e.g., $R = TP/(TP + FN)$. A higher recall score suggests that the algorithm effectively detects most cells in the image, with fewer missed detections. The F1 score combines precision and recall via their harmonic mean, offering a balanced view of the accuracy and sensitivity, e.g., $F1score = 2 \times (P \times R)/(P + R)$. The F1 score is particularly valuable when there is an imbalance between FP's and FN's, as it considers both. It emphasizes the importance of high values in both P and R metrics. Hence, a higher F1-score indicates that the algorithm is both accurate and comprehensive in cell detection.

For evaluating the performance of the proposed algorithm across varying cell densities, two cell lines, e.g., HEK 293 and CHO DG44, were prepared at seven distinct densities between 20×10^3 and 10×10^6 cells/mL

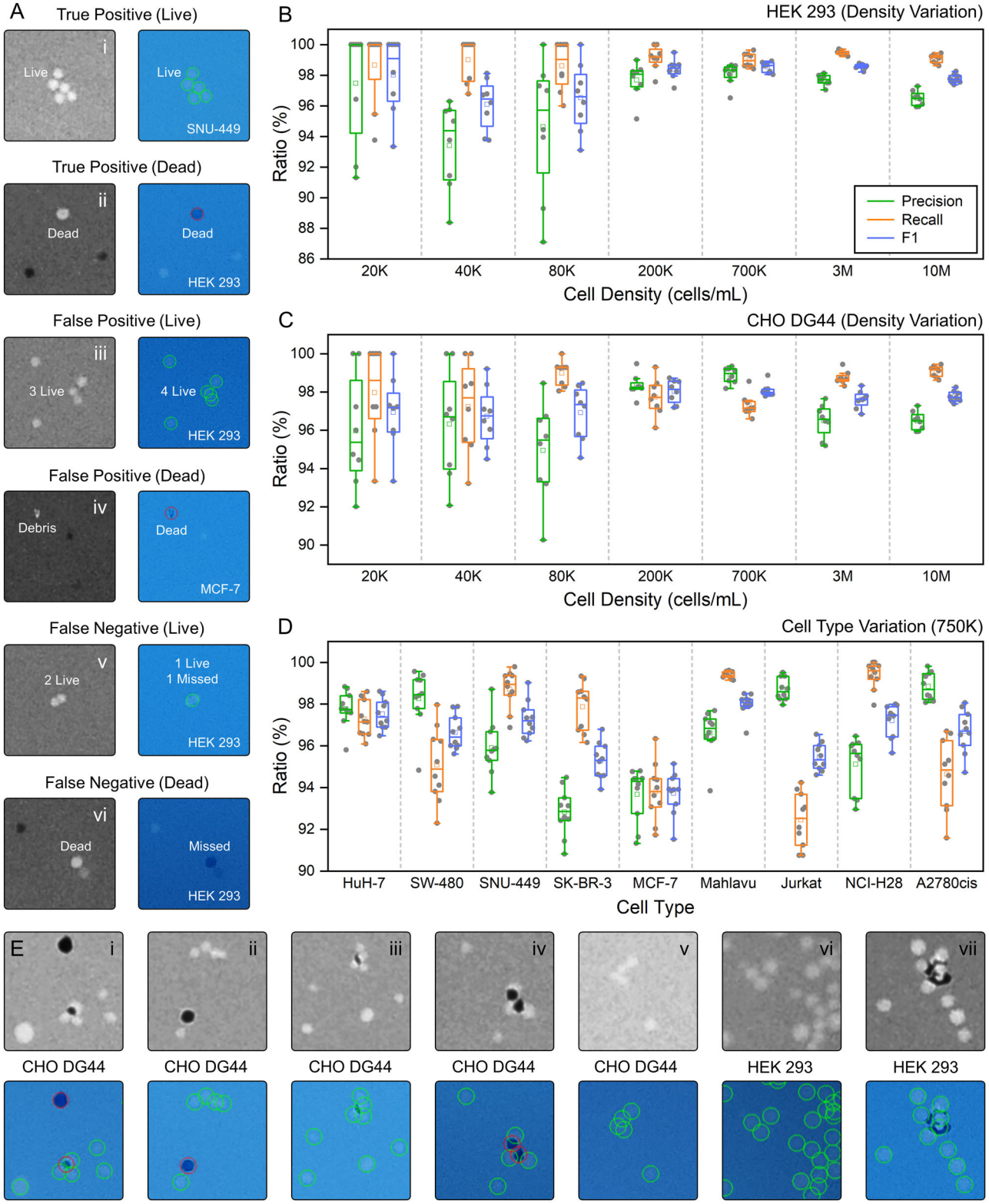

Fig. 3 | Performance study for evaluating live and dead cell identification. **A** Examples illustrating the definitions used for confusion matrices in live and dead cell identification. True Positives (TP) represent cells correctly identified as live or dead; False Positives (FP) occur when non-cell regions are incorrectly identified as containing cells, and False Negatives (FN) are cells that were missed by the algorithm. Calculated performance metrics, e.g., precision (green), recall (orange), and F1 score (purple), for (**B**) HEK 293 and (**C**) CHO DG44 cells across a wide range of cell densities, e.g., 20×10^3 to 10×10^6 cells/mL, based on n = 8 replicates. **D** Performance metrics calculated for different cell types under a cell density of 750×10^3 to 820×10^3 cells/mL, with $n = 10$ replicates. The box plots represent interquartile ranges, and the squares indicate average values. **E** Examples of challenging conditions where the image-processing algorithm identifies live and dead cells. Grayscale represents the enhanced images, and the blue-color illustrates the cell segmentation images.

with eight replicates, where each replicate involves the capture of a single image. Figure 3B, C displays the three performance parameters, e.g., Precision (green), Recall (orange), and F1 score (purple), for HEK 293 and CHO DG44 cells, respectively, across varying cell densities. As expected, the performance improves with increasing cell density, indicating better accuracy as the number of cells counted increases. This improvement is attributed to the fact that the contribution of false positives or false negatives to the percentage error diminishes in larger sample pools, resulting in more reliable and robust performance at higher cell densities. For HEK 293 cells, the mean Precision, Recall, and F1-score were calculated within the ranges of 93.4–98.1%, 98.6–99.5%, and 96.1–98.6%, respectively. For CHO DG44 cells, these parameters are in the ranges of 94.9–98.9%, 97.2–99.1%, and 96.7–98.1%, respectively.

The adaptability of the proposed algorithm to various cell types is further evaluated using HuH-7, SW-480, SNU-449, SK-BR-3, MCF-7, Mahlavu, Jurkat, NCI-H28, and A2780cis cells (Fig. 3D). For each cell type, experiments were conducted within a density range of 750×10^3–820×10^3 cells/mL, ensuring robustness across a broad spectrum of samples. Each test includes ten replicates, with a single image captured per replicate, to assess the performance in detecting and analyzing different cellular morphologies and densities. Across different cell types, the mean Precision, Recall, and F1 scores were calculated in the range between 92.8% and 98.8%, 92.5% and 99.4%, and 93.7% and 98%, respectively. These results strongly highlight that the proposed algorithm is robust and reliable in accurately detecting live and dead cells across a diverse range of cell lines. This high accuracy translates to exceptional resolution in distinguishing live and dead cells even under challenging conditions. For instance, Fig. 3E demonstrates several scenarios where Qtouch accurately performs cell identification: (i) One dead CHO DG44 cell is identified within a cluster of three live cells. (ii) A cluster of four CHO DG44 cells. (iii) Four CHO DG44 cells in contact with a debris particle. (iv) Accurate identification of three live and two dead CHO DG44 cells in a cluster. (v) Resolution of a cluster of four CHO DG44 cells into individual cells. (vi) Precise detection of individual cells within a bulk cluster of HEK 293 cells. (vii) Differentiation of a cluster of six HEK 293 cells partially covered by a large debris particle.

Quantella delivers accurate cell density and viability data

Quantella enables precise quantification of cell densities, ensuring minimal variation across replicates, a critical factor for reproducibility in high-throughput biological studies. To underscore its robustness and reliability, we conducted comprehensive evaluations using two distinct cell lines, e.g., HEK 293 and CHO DG44, across an extensive cell density spectrum, ranging from 20×10^3 to 20×10^6 cells/mL. We used flow cytometry, the gold standard in cell counting, as a reference to evaluate Quantella's performance, alongside manual cell counting for comparison. Manual cell counting was performed using a Thoma hemocytometer (ISOLAB Laborgerate GmbH), and the cell images were observed with an inverted microscope (Carl Zeiss™ Axio Vert.A1). For both Quantella and manual cell counting, the cell suspension was mixed with a trypan blue solution (0.4%, Gibco™) in a 1:1 ratio to assess cell viability. For flow cytometry measurements, propidium iodide (PI) DNA staining (Sigma-Aldrich®) was prepared by dissolving PI in PBS at a concentration of 1 mg/mL, and subsequently mixed with the cell suspension. The measurements were conducted using the NovoCyte Advanteon flow cytometer (Agilent Technologies, Inc.), and cell concentration and viability parameters were assessed using the NovoExpress software. All comparison studies were conducted using double-blind tests.

As shown in the box plots displayed in Fig. 4A (HEK 293), B (CHO DG44), the cell density measurements from eight replicates obtained using Quantella (green) are compared with those from manual counting (blue) and flow cytometry (orange), highlighting Quantella's consistency and accuracy. The quality of our results was demonstrated using mean error (bar plots) and SD analyses (solid squares). In the mean error analysis, expressed as a percentage, we evaluated the deviation of the mean values obtained from Quantella and manual counting methods relative to the results from flow cytometry. For the SD analysis, we reported the SD solely for the selected methods, e.g., Quantella or manual counting, excluding variability arising from the flow cytometry measurements, which is primarily attributed to the inherent variation in the prepared cell samples. To isolate the real SD due to the selected method itself, we calculated the real SD by subtracting the variance of the flow cytometry method from that of the selected method. The real SD was determined using the following formula, e.g., $Real\ SD = \sqrt{SD^2_{Method} - SD^2_{Flow}}$

We interpreted the results for two distinct groups, e.g., standard cell density (up to 10×10^6 cells/mL) and very high cell density. For the standard cell density, we determined a mean error of less than 6% for HEK 293 and less than 3% for CHO DG44 using Quantella, while manual counting showed errors ranging from 3 to 19% for HEK 293 and from 2 to 25% for CHO DG44. On the other hand, the SD values for Quantella were calculated to the range between 8 and 25% for HEK 293 and between 4 and 32% for CHO DG44, while manual counting yielded SD values between 15 and 65% for HEK 293 and between 21 and 42% for CHO DG44. For high cell density, manual cell counting based on hemocytometry fails due to cell overlap, creating clusters that are difficult to distinguish with naked eye. As shown in Fig. 4C, which illustrates HEK 293 cells at densities of 10×10^6 and 20×10^6 cells/mL, the clustering of cells makes manual counting challenging. Therefore, Fig. 4A, B do not represent manual counting results for these cell densities. Quantella, however, does not face this issue due to its high performance in distinguishing individual cells. For example, we determined the mean error with Quantella to be 4.2 (10×10^6 cells/mL) and 13.9% (19×10^6 cells/mL), with SD values of 4.6% (10×10^6 cells/mL) and 10.6% (19×10^6 cells/mL) for HEK 293 cells. For CHO DG44, the mean error was 6.3% (10×10^6 cells/mL) and 2.8% (18×10^6 cells/mL), with SD values of 2.7% (10×10^6 cells/mL) and 3.8% (18×10^6 cells/mL). As expected, high cell densities can introduce variability in measurements, even with the gold standard flow cytometry, often necessitating further sample dilution. In contrast, Quantella's error rate and SD do not have a direct relation to cell density, eliminating the need for pre-counting dilutions. This approach minimizes potential errors linked to dilution steps, which are sometimes required in other cell counting methods[23].

To demonstrate the high performance of Quantella in determining cell viability, we studied samples with varying viability percentages, ranging from 70 to 94%. We compared the results obtained from Quantella (green) and manual cell counting (blue) with flow cytometry (orange). The box plots in Fig. 4D show the viability results for five different cell densities of CHO DG44 cells, ranging from 80×10^3 to 3×10^6 cells/mL. In these experiments, cell viability and cell density were not correlated, ensuring that the number of cells did not affect the accuracy of viability calculations for each method. The mean errors (bar plots) for Quantella were determined to be between 0.05 and 1%, while manual cell counting yields errors ranging from 2 to 12%. Quantella's superior performance is further evident in the SD values (solid squares), which range from 0.7 to 11.6%, compared to manual counting, which has SD values between 1.5 and 17%. Given the higher SD values observed in certain samples, Quantella leverages its imaging-based approach with a large FOV and ability to scan the entire flow cell, enabling comprehensive and accurate viability assessments (see "Methods" section for the details of the calibration study with Quantella, manual counting, and flow cytometry).

Quantella allows confluency calculation

Quantella offers confluency calculations by generating high-contrast cell images through the integration of a custom-designed grid slab. Figure 5A illustrates the working principle of this grid slab, which consists of a white paper printed with black grids placed between five microscope slides (see photograph), e.g., four glass slides above the paper and one underneath, all securely glued together to ensure stability and alignment. The combination of the 4 mm thickness of the grid slab and the 3 mm acrylic layer of the flow cell creates a total distance of 7 mm between the samples and the grid. This design enables the generation of a high-contrast background without capturing the grid itself in the imaging process. The black grids enhance the

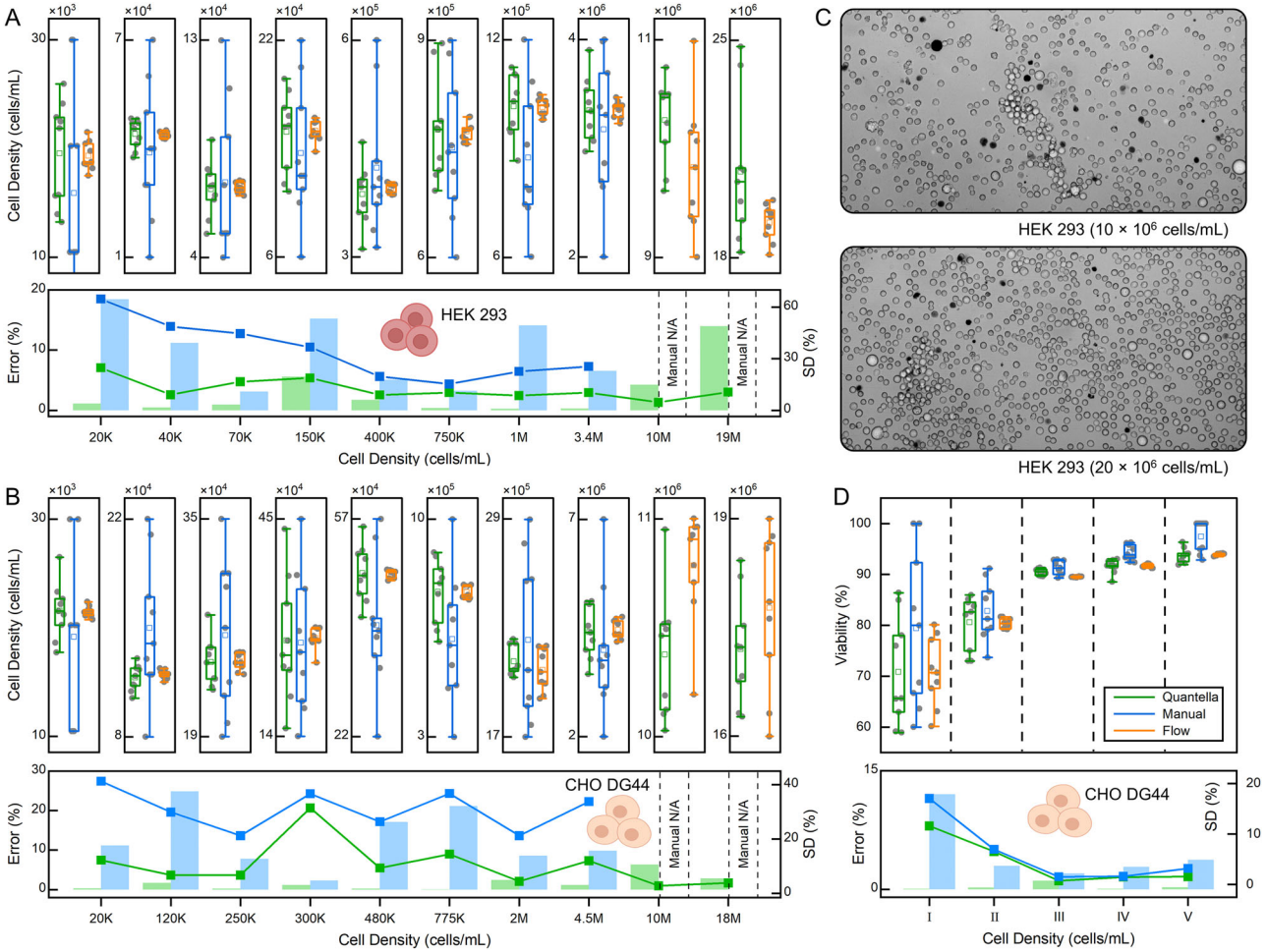

Fig. 4 | Cell density and viability calculations. Cell density values determined for (**A**) HEK 293 and (**B**) CHO DG44 cells at different cell densities. Top figures: Cell density values measured using Quantella (green), manual cell counting (blue), and flow cytometry (orange). Bottom figures: Mean error (green/blue bars: Quantella/Manual counting) and SD values (green/blue squares: Quantella/Manual counting) calculated by comparing the cell density results of each method with flow cytometry. **C** The image of HEK 293 cells at densities of 10×10^6 and 20×10^6 cells/mL. **D** Top figure: Cell viability values determined for CHO DG44 cells at different cell densities using Quantella (green), manual cell counting (blue), and flow cytometry (orange). Bottom figure: Mean error (green/blue bars: Quantella/Manual counting) and SD values (green/blue squares: Quantella/Manual counting) calculated by comparing the viability results of each method with flow cytometry. The box plots represent the interquartile ranges, and the squares indicate the average values of the data for $n = 8$ (for density analysis), 9 (for viability analysis) replicates.

visibility of transparent cells by highlighting their edges and features. By creating areas of varying light intensity, where light either passes through or is blocked by the grid, we improved the detection of otherwise transparent regions. This technique works similarly to phase contrast or differential interference contrast microscopy[24], enhancing contrast and making transparent samples more distinguishable from the background. Figure 5B demonstrates how the grid creates a strong contrast to highlight the positions of the cells near the grid that are imaged with better clarity, while the areas further from the grid (illuminated with the white LED) show more transparent cells that are barely visible. Figure 5C presents the comparison between the same sample of MCF-7 cells imaged using phase contrast microscopy (Olympus CKX41) and Quentalla, clearly demonstrating Quentalla's high-contrast imaging capability with a much simpler and more cost-effective methodology (see "Methods" section for the experimental details of the confluency analyses).

Image segmentation for confluency analysis

Figure 5D shows the flowchart illustrating the workflow of the proposed image segmentation algorithm for confluency analysis. In the preprocessing step, the input image, with dimensions of $4000 \times 3000 \times 3$ pixels (8 bits per pixel), undergoes filtering with a 2D Gaussian smoothing filter (an empirically determined SD = 2) to mitigate noise and possible artifacts introduced by JPEG compression. Subsequently, two distinct filtering techniques, e.g., variance filter and entropy filter, are applied to enhance image features for segmentation. To emphasize regions with significant intensity variations, e.g., textures, corners, and edges, the local variance information is extracted from the image[25]. The variance filter effectively enhances the visibility of cell boundaries, as these regions exhibit sharp intensity variations in the image. This filter computes the local variance in a small neighborhood of each pixel within the Gaussian-smoothed image. In the developed segmentation algorithm, as small as a 3×3 neighborhood (matrix size is empirically determined) is extracted for each target pixel (i.e., centering pixel in the neighborhood), and the variance of these nine pixels are computed and assigned as the output value of the centering pixel in the neighborhood. Consequently, each output value represents the variance of its local neighborhood, highlighting the areas of high intensity variation. Subsequently, gamma transformation with $\gamma = 0.6$ is applied to adjust the illumination, and enhance the contrast of the variance filtered output. Following this step, the final values are normalized to a range of [0, 255] to ensure uniform intensity scaling[26].

To identify intensity variations corresponding to cell boundaries, the gradient magnitude of the resulting image is calculated via Sobel operators[27]. Sobel operators apply two 3×3 kernels to approximate the image gradients in the horizontal (x) and vertical (y) directions, thereby highlighting the

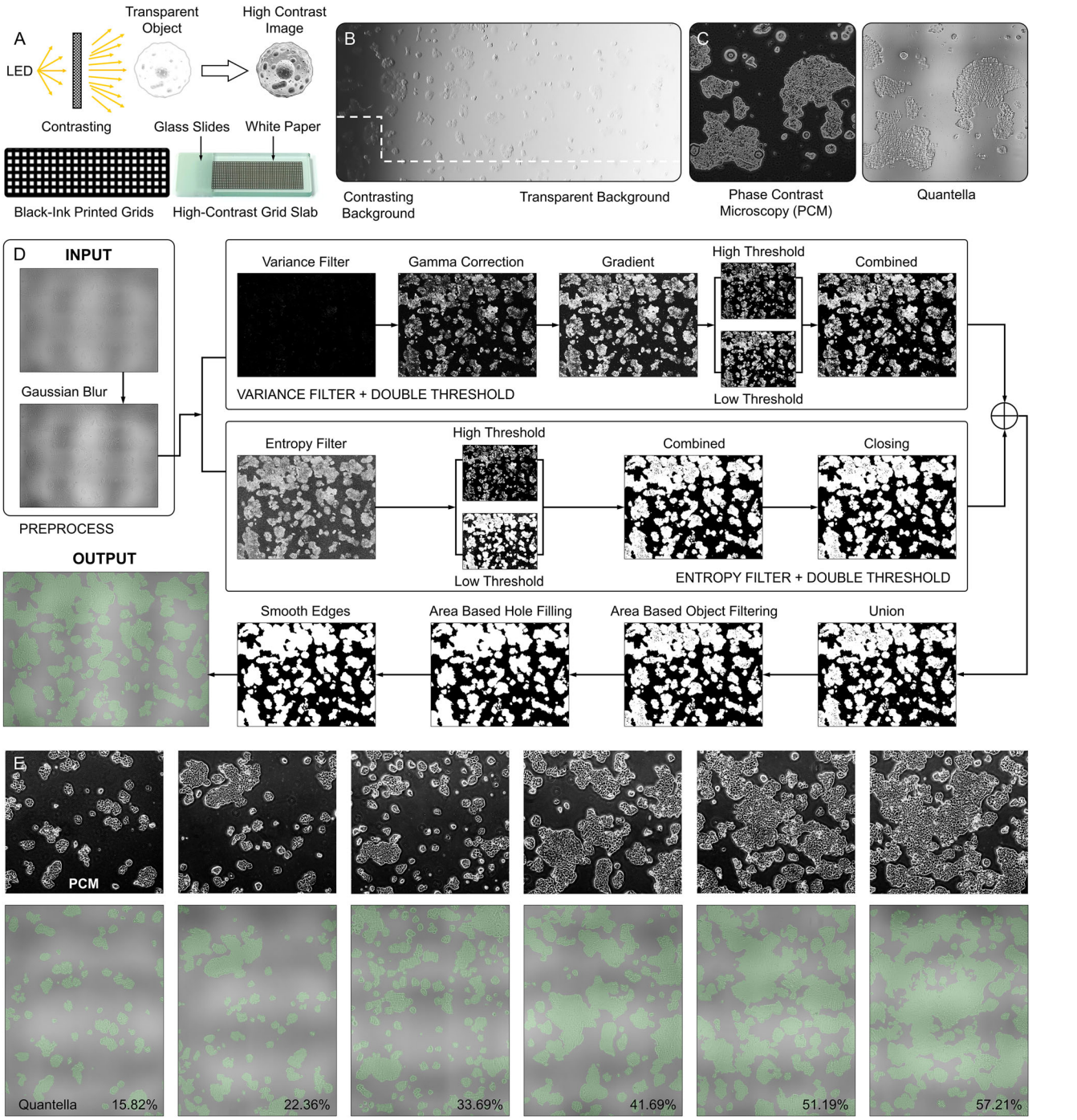

Fig. 5 | Image segmentation algorithm for confluency analysis feature of Quantella. A Schematic representation of the grid slab's working principle, illustrating how it generates a high-contrast background to enhance cell visibility for accurate confluency calculations. **B** Visualization of how transparent cells become distinguishable, with edges and features highlighted against a contrasting background created by the grid slab, compared to a transparent background. **C** High-contrast confluency images produced by Quantella, offering visibility similar to phase-contrast microscopy (PCM). **D** Flowchart depicting the workflow of the image segmentation algorithm developed for confluency analysis. **E** Confluency analysis results for MCF-7 cell samples with varying confluency levels, together with their PCM images.

areas of rapid intensity change indicative of cell boundaries.

$$G_x = \begin{bmatrix} 1 & 0 & -1 \\ 2 & 0 & -2 \\ 1 & 0 & -1 \end{bmatrix}, G_y = \begin{bmatrix} 1 & 2 & 1 \\ 0 & 0 & 0 \\ -1 & -2 & -1 \end{bmatrix} \quad (3)$$

Here, G_x and G_y are the gradient extraction kernels along the x- and y-directions, where their magnitude at each pixel location (i, j) is calculated via the Pythagorean sum as:

$$G_{mag}(i,j) = \sqrt{G_x(i,j)^2 + G_y(i,j)^2} \quad (4)$$

The gradient image (G_{mag}) is normalized to a range of [0, 255] to ensure uniform intensity scaling, and then subjected to double thresholding using the hysteresis thresholding technique. This approach allows for more effective segmentation of cell boundaries and finer details by leveraging two intensity thresholds to distinguish strong edges while preserving weaker, connected edges. With this method, the strongest edges are isolated, noise is removed, and only prominent edges remain using a higher threshold serving as "marker" (set to 0.8), while a lower threshold serving as "mask" (set to 0.5), which captures finer details and weaker edges. These threshold values were empirically optimized across a diverse set of images to balance edge sensitivity with robustness against noise and lighting variability, particularly in smartphone-acquired datasets. The two output images are then combined with morphological reconstruction to refine edge detection. This approach facilitates precise segmentation of cell boundaries by combining robust edge information with enhanced details, balancing noise/artifacts reduction and detail preservation.

An entropy filtering-based approach is also proposed in this study to further support the outcomes from the variance filtering technique. The entropy filter is a widely used technique for quantifying the randomness or variability in local pixel intensity[28]. This method assigns higher values to regions with significant intensity variation, highlighting areas rich in information, such as edges, corners, and textures. In other words, any uniform intensity of the background results in low entropy values, while the complex textures and varying intensities of cells yield higher entropy values, which facilitate the identification of cell boundaries by distinguishing them from the relatively uniform background. In this study, this filter is implemented by calculating the local entropy using a 9×9 local neighborhood (matrix size is empirically determined) around each target pixel. The filtering output is double thresholded with empirically determined values, e.g., 0.7 and 0.4, to segment regions of varying intensity, and the output images are combined with morphological reconstruction, followed by a morphological closing operation using a disk-shaped kernel with a radius of 3. The closing operation effectively fills small holes within cell boundaries, enhancing the segmentation and ensuring the integrity of the detected cell structures.

The binary outputs of variance and entropy filters are later combined through a "union" operation to create a unified segmentation result. To refine this output, area-based object filtering is applied to remove small-connected objects, such as debris, with a connectivity value of 8. Subsequently, area-based hole filling is employed to fill the interiors of the detected cell boundaries, ensuring completeness in segmentation. To further enhance the output, the cell boundaries are smoothed using a mean filter with a window of size 21. The final processed image is then converted to RGB colorspace, with the detected cells highlighted in green as a mask. This mask is overlaid on the input image to label the identified cells clearly and visually. Finally, confluency (%) is determined by dividing the number of white pixels by the total number of pixels in the final binary output image, e.g., *White Pixels*/*Total Pixels*. Figure 5E presents the analysis results for MCF-7 cell samples with different confluency levels together with their phase contrast microscopy images (see Algorithm 4), demonstrating the high computational accuracy of our algorithm.

Algorithm 4. Confluency Calculation and Segmentation

Require: Input image I_{input}

Ensure: Labeled segmentation map $I_{labeled}$, confluency percentage *Confluency*

function ConfluencyAnalysis(I_{input})
  $I_{gray} \leftarrow$ ConvertToGrayscale(I_{input})
  $I_{smoothed} \leftarrow$ ApplyGaussianFilter(I_{gray}, $\sigma = 2$)
  $I_{normalized} \leftarrow$ ScaleIntensity($I_{smoothed}$, [0, 255])
  $I_{variance} \leftarrow$ LocalVarianceFilter($I_{normalized}$)
  $I_{enhanced} \leftarrow$ GammaCorrection($I_{variance}$, $\gamma = 0.6$)
  $G_{mag} \leftarrow$ ComputeGradientMagnitude($I_{enhanced}$)
  T_{high}, $T_{low} \leftarrow$ 0.8, 0.5
  $I_{highEdges} \leftarrow G_{mag} > T_{high}$
  $I_{lowEdges} \leftarrow G_{mag} > T_{low}$
  $I_{edgeMask} \leftarrow$ MorphologicalReconstruction($I_{highEdges}$, $I_{lowEdges}$)
  $I_{entropy} \leftarrow$ ComputeEntropyFilter($I_{normalized}$, 9×9)
  $I_{combined} \leftarrow I_{edgeMask} \vee I_{entropy}$
  $I_{filtered} \leftarrow$ RemoveSmallRegions($I_{combined}$, 1000)
  $I_{filled} \leftarrow$ FillSmallHoles($I_{filtered}$, 5000)
  $I_{smoothedEdges} \leftarrow$ SmoothBinaryEdges(I_{filled}, 21)
  $N_{total} \leftarrow$ PixelCount($I_{smoothedEdges}$)
  $N_{foreground} \leftarrow$ CountForegroundPixels($I_{smoothedEdges}$)
  $Confluency \leftarrow (N_{foreground} / N_{total}) \times 100$
  $I_{mask} \leftarrow$ CreateGreenMask($I_{smoothedEdges}$)
  $I_{overlay} \leftarrow$ OverlayMaskOnImage(I_{gray}, I_{mask}, 0.1)
  return $I_{overlay}$, *Confluency*
end function

Quantella in life science applications

In this section, we demonstrate Quantella's versatile capabilities across a range of biological applications, including confluency, viability, and cell density tracking. Through advanced imaging and detection methods, Quantella has been utilized to assess drug effects on cells, monitor cell growth under varying conditions, and perform precise RBC counting.

Quantella facilitates drug effect analysis through high-contrast morphological imaging and confluency tracking

Quantella enables detailed monitoring of drug effects on cells, ensuring high precision and clarity in capturing morphological changes, a critical factor for assessing drug efficacy. To demonstrate this capability, we investigated the antitumor effects of Paclitaxel (PTX), a standard-of-care drug, and monitored its antitumor activity on MCF-7 cells through confluency images. Figure 6A illustrates the mechanism of the action of PTX. PTX interferes with the normal breakdown of microtubules during cell division, causing mitotic arrest in the prometaphase stage. This disruption leads to gross spindle defects, ultimately resulting in cell death[29]. The figure shows the clear morphological differences between the control and treated groups after 24 h of exposure to 1 μm PTX. The treated cells exhibit swelling, a characteristic feature of cell death, which is not observed in the control group. Capturing these high-contrast images not only enables the observation of morphological changes but also allows for quantifying the reduction in confluency induced by PTX treatment. As shown in Fig. 6A, the control group has a confluency of 40.84%, while the PTX-treated group exhibited a significantly reduced confluency of 16.61%, indicating the drug's effectiveness in inhibiting cell proliferation (see "Methods" section for the experimental details of the PTX study). This capability has important implications for cancer research and personalized medicine. By enabling quantitative assessment of drug-induced morphological changes and proliferation arrest, Quantella supports preclinical drug screening workflows that require rapid, low-cost, and label-free evaluation of therapeutic efficacy. The ability to detect early cytostatic effects could aid in identifying drug responders and non-responders, making it particularly valuable in contexts such as patient-derived tumor models or resource-limited clinical research settings.

Quantella enables comprehensive drug impact assessment via viability tracking

Quantella also allows for precise monitoring of the impact of therapeutic agents on cell survival, which offers high-resolution insights into the effects of different drug concentrations. To demonstrate this capability, we investigated the cytotoxic effects of doxorubicin hydrochloride (DOX), a commonly used chemotherapeutic agent, and tracked its influence on cell viability over time for different concentrations. Figure 6B illustrates the mechanism of the action of DOX. DOX works by intercalating into DNA strands, disrupting essential DNA replication processes, which induce double-strand breaks, leading to significant DNA damage. This damage triggers apoptosis, a form of programmed cell death. The mechanism also involves the generation of reactive oxygen species, which further contribute to DNA damage and cytotoxicity in cancer cells[30]. Figure 6B shows the viability of Jurkat cells under different

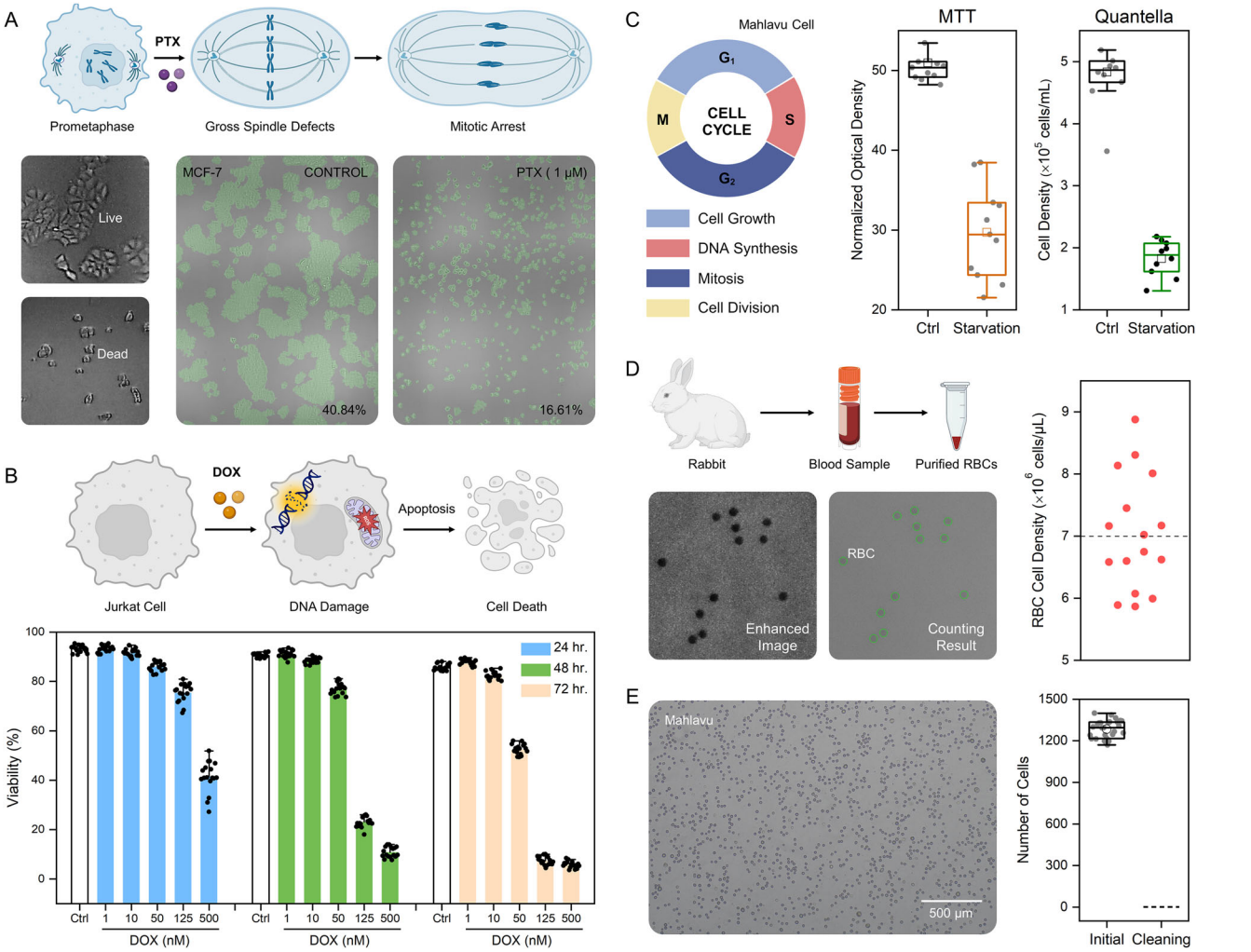

Fig. 6 | Quantella in life science applications. A Schematic illustration of the working principle of PTX. The captured images of MCF-7 cells demonstrate the healthy cell formation, which is degraded upon the PTX exposure. The decrease in cell confluency demonstrates PTX's (1 μm) antitumor effect. **B** Schematic illustration of the working principle of DOX. The bar plot shows the decrease in cell viability at different concentrations of DOX for treatment durations of 24 (blue), 48 (green), and 72 h (peach) for different drug concentrations, e.g., 1 nM, 10 nM, 50 nM, 125 nM, and 500 nM compared to the control group (white). In the figure, the error bars represent twice the standard deviation of $n = 17$ replicates. Calculated p-values (Control vs. Treated groups) are as follows, e.g., for the 24 h treatment: 0.8 (1 nM), 5.1×10^{-3} (10 nM), 1.3×10^{-9} (50 nM), 1×10^{-11} (125 nM), 7.9×10^{-16} (500 nM), for the 48 h treatment: 0.1 (1 nM), 8.2×10^{-6} (10 nM), 7×10^{-14} (50 nM), 2.8×10^{-24} (125 nM), 4.8×10^{-26} (500 nM); and for the 72 h treatment: 5.4×10^{-5} (1 nM), 4.2×10^{-5} (10 nM), 2×10^{-19} (50 nM), 2.3×10^{-26} (125 nM), 3×10^{-28} (500 nM). **C** Schematic illustration of the phases in the cell cycle. Box plots show cell density changes for 48 h serum starvation, measured by MTT ($n = 11$) and Quantella ($n = 10$). Control = Black, Starvation (MTT/Quantella) = Orange/Green. Cohen's d values calculated for the MTT assay and Quantella are 4.60 and 6.47, respectively. **D** Schematic illustration of RBC extraction from a rabbit. Left: Image of RBCs enhanced via the image-processing algorithm. Right: Location of cells (highlighted with green) determined by the image-processing algorithm. The figure shows the cell density of the same RBC samples calculated via Quantella with $n = 17$ replicates (red circles), each containing 20 sample images. The black dashed line highlights the hemogram result, where Quantella yields only a 0.14% mean error deviation from the hemogram result. **E** Image of Mahlavu cells injected into the flow cell at a density of 2.5×10^6 cells/mL. The accompanying box plot demonstrates that the cleaning protocol effectively removes all residual cells. The box plots represent interquartile ranges, and the squares indicate average values.

DOX concentrations (1 nM, 10 nM, 50 nM, 125 nM, and 500 nM) across 24 (blue bars), 48 (green bars), and 72 h (peach bars) time points, along with the control group (white bars). Quantella accurately captured the decrease in cell viability with increasing concentrations of DOX, as well as the time-dependent changes observed over these intervals (see "Methods" section for the experimental details of the DOX study).

This further reduction in cell viability due to increasing drug concentration and treatment duration was also confirmed through Welch's t-test at a 5% significance level (where α is between 0 and 1), such that no significant difference could be detected if $p > 0.05$. For the 24 h time point, the p-values for the comparisons between the control group and increasing concentrations of DOX are, e.g., p(Control vs. Treated groups) = 0.8 (1 nM), 5.1×10^{-3} (10 nM), 1.3×10^{-9} (50 nM), 1×10^{-11} (125 nM), 7.9×10^{-16} (500 nM). For the 48 h time point, p-values were 0.1 (1 nM), 8.2×10^{-6} (10 nM), 7×10^{-14} (50 nM), 2.8×10^{-24} (125 nM), 4.8×10^{-26} (500 nM). Finally, for the 72 h time point, p-values were 5.4×10^{-5} (1 nM), 4.2×10^{-5} (10 nM), 2×10^{-19} (50 nM), 2.3×10^{-26} (125 nM), 3×10^{-28} (500 nM). These p-values confirm the significant impact of higher DOX concentrations and longer treatment durations on cell viability. This type of viability tracking is highly relevant for pharmacological profiling in oncology and drug discovery workflows, where time- and dose-dependent cytotoxicity data guide therapeutic index estimation and optimization of treatment regimens. Quantella's ability to sensitively detect viability loss over time provides a valuable alternative to conventional methods like MTT or trypan blue exclusion assays, especially in high-throughput settings. Its integration of real-time analysis and minimal manual input makes it particularly suitable for evaluating candidate drugs during early preclinical testing or for repurposing screens in personalized treatment planning.

Quantella enables accurate cell growth monitoring under serum starvation conditions via cell density analysis

To demonstrate Quantella's ability to monitor cell growth and assess intracellular pathways, we investigated the effect of serum starvation on cell proliferation. Figure 6C illustrates the phases in the cell cycle. Serum starvation causes a reversible arrest in the G1 phase of the cell cycle, halting cell growth due to the absence of growth factors. Cells in this state do not progress to the S/G2/M phases until serum is reintroduced[31]. In this experiment, we cultured cells in complete medium containing 10% fetal bovine serum and serum-free medium for 48 h. In the double-blind tests, Quantella was used to measure cell density (Control/Starvation = Black/Orange) and compared to results obtained using the MTT assay (Control/Starvation = Black/Green), which measures optical density. The results from both Quantella and MTT show a significant reduction in cell growth under serum starvation, confirming the arrest in cell multiplication (see "Methods" section for the experimental details of the serum starvation study).

For a quantitative comparison, Cohen's *d* analysis was chosen. Cohen's *d* is a widely accepted statistical measure for direct comparison of the magnitude of differences between two groups, in this case, control and starvation conditions. This method is ideal for our study as it provides a standardized way to assess how each method detects the impact of starvation on cell density. By calculating Cohen's *d*, we can determine the significance of the differences between conditions and compare the sensitivity of MTT and Quantella in detecting those differences. A larger Cohen's *d* indicates a more pronounced effect, making the method an appropriate metric to highlight the superior sensitivity and precision. To calculate Cohen's *d*, we used the following formula, $d = \frac{\bar{x}_{Ctrl} - \bar{x}_{star}}{SD_{pooled}}$ where $\bar{x}_{Ctrl}$ and $\bar{x}_{star}$ are the mean of control and starvation groups, respectively. Here, the pooled SD was calculated by combining the SD of the control and starvation groups, e.g., $SD_{pooled} = \sqrt{\frac{SD_{ctrl}^2 + SD_{star}^2}{2}}$. For MTT, the Cohen's *d* is calculated as 4.60, while the Cohen's *d* for Quantella is 6.47, which reflects a much larger reduction in cell viability. This suggests that Quantella is more sensitive in detecting the impact of serum starvation, capturing a more pronounced difference between control and starvation conditions than MTT. The higher Cohen's *d* for Quantella highlights its superior ability to monitor changes in cell density, offering more precise insights into cell growth dynamics under varying conditions.

From a biomedical perspective, the ability to accurately detect cell cycle arrest through label-free density measurements is vital in cancer biology, regenerative medicine, and metabolic research. Quantella's sensitivity in identifying serum deprivation-induced quiescence offers a valuable tool for investigating nutrient-dependent signaling pathways, screening metabolic modulators, or optimizing stem cell culture conditions. In clinical research, such monitoring could help evaluate cellular responses to starvation-mimicking treatments, such as caloric restriction or mTOR inhibitors, which are gaining interest in oncology and aging research.

Quantella enables accurate red blood cell counting through high-precision imaging and detection

We demonstrated the successful imaging of RBCs from a rabbit (Tv67, 45-week-old New Zealand breed), with an average cell size of ~6 μm (see "Methods" section for the RBC preparation). Quantella's imaging capabilities allowed for high-contrast visualization of these cells, as seen in the enhanced image (Fig. 6D-left). Our automated cell detection algorithm, as shown in the counting result (Fig. 6D-right), precisely identified the RBCs within the sample. The figure also shows the cell density of RBCs from the same sample, with 16 replicates of the experiment (red circles), each containing 20 sample images, which yields an RBC density of 7.03×10^6 cells/μL. In the double-blind test, this value was compared with the hemogram result of 7.02×10^6 cells/μL (highlighted with black dashed line), yielding a low mean error of only 0.14%.

Accurate and rapid RBC counting is a cornerstone of hematological diagnostics, aiding in the detection of anemia, polycythemia, and other blood disorders. Quantella's ability to deliver high-precision RBC counts comparable to clinical-grade hemogram systems, with minimal equipment and operator expertise, suggests its potential for use in point-of-care testing, especially in low-resource settings. This capability could support decentralized diagnostics in veterinary and human health applications alike, enabling routine monitoring in clinics, field hospitals, or remote laboratories where traditional automated hematology analyzers are inaccessible or cost-prohibitive.

Dual-mode flow cell

Quantella offers two versatile modalities for utilizing its flow cell, e.g., single- and multi-use, addressing diverse experimental needs. The single-use mode provides a highly cost-effective solution, with each flow cell manufactured at a cost of ~$0.20 USD. This mode is particularly advantageous for applications requiring strict sterility, such as working with highly sensitive or unique samples, where avoiding cross-contamination is critical. On the other hand, multi-use mode provides a cost-efficient and sustainable solution for routine analyses or high-throughput experiments. For multi-use applications, the flow cell surface is coated with Dulbecco's Modified Eagle Medium (DMEM) supplemented with 10 μg/mL Polyethylene Glycol 8000 (PEG 8000, CAS 25322-68-3) and 5 mM Ethylenediaminetetraacetic acid (EDTA) to prevent cell adhesion. To enable multi-use functionality, the flow cell was rinsed with PBS (1X) and DI water to eliminate cells adherence and residual media. Figure 6E shows the microcopy image of ~1300 Mahlavu cells in a 2.9 mm × 1.9 mm wide FOV. The box plot in the same figure shows the average cell count from 26 different locations with the same FOV on the flow cell, confirming that the cleaning protocol effectively removes all residual cells. The flexibility of these two modes highlights Quantella's adaptability to diverse experimental demands, e.g., sterility and sustainability.

Smartphone application for automated cell analysis

Qtouch, developed in Flutter, communicates with a cloud server hosting advanced image-processing scripts, ensuring an efficient and intuitive workflow for diverse experimental needs. Figure 7A shows the workflow of Qtouch. As shown in Fig. 7B, operators can initiate the experiments by selecting the desired analysis type, e.g., "Cell Counting" (cell density and viability) or "Confluency". As shown in Fig. 7C, the "Camera" feature captures high-resolution images, which can be reviewed via the "View Images" interface. Specific images for analysis are selected using the "Select Images" option and transmitted to the cloud server for processing through the "Process Images" button. For cell density and viability measurements (Fig. 7C), Qtouch provides real-time control over the piezoelectric pump, managed by the microcontroller via PWM signals. Commands such as "Start" and "Stop" are sent via Bluetooth, enabling smooth and controlled liquid flow during experiments. Results, including cell density and viability values for individual images and their averages, are processed by the cloud server and returned to Qtouch for real-time visualization. For confluency analysis (Fig. 7D), which does not require liquid handling, Qtouch streamlines the interface by including only image capture and selection options. Results are provided as confluency percentages for individual images and their overall averages. The server, implemented using Flask, acts as the intermediary between Qtouch and the image processing scripts. Uploaded images are stored in the designated directories, with all requests and operations logged for traceability and debugging. Based on the experiment type, the server triggers the appropriate executable files compiled from MATLAB scripts to perform image analysis. Results, including labeled images and quantitative data, are saved and transmitted back to Qtouch for display. Since the MATLAB license is required only during the development phase for coding and algorithm optimization, the cloud-based architecture ensures cost-effective system operation. Image processing and data analysis are performed using compiled executables generated from MATLAB scripts, eliminating the need for active MATLAB licenses during routine experiments. This approach enables operation without direct MATLAB access, ensuring that all image-processing tasks run independently on the cloud server.

At the end of each experiment, users can initiate the cleaning process to rinse the chamber and tubing with a cleaning solution using the pump

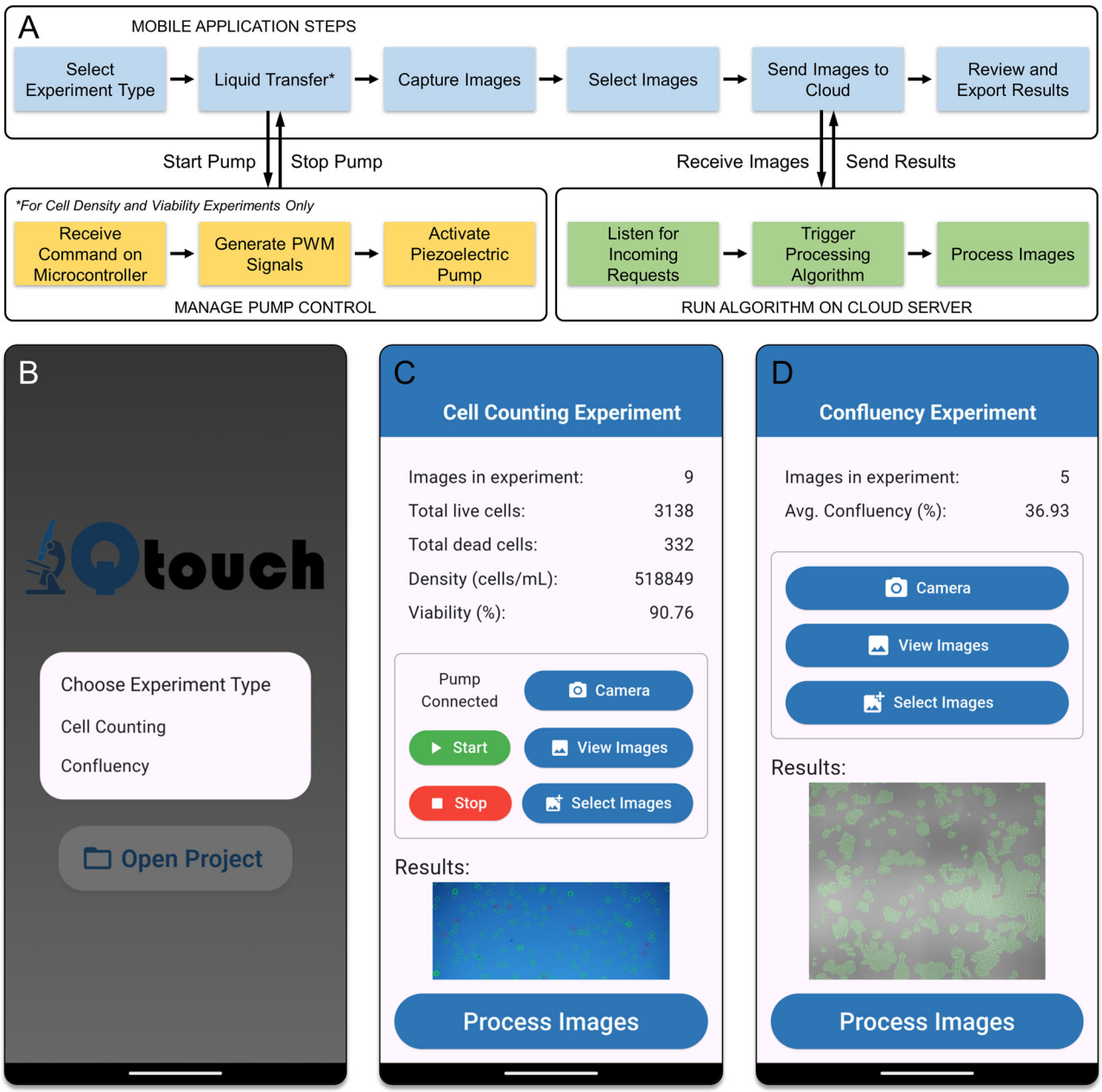

Fig. 7 | Smartphone application for hardware control and data acquisition and processing. A Qtouch workflow for imaging, pump control, communication with the server for data processing, and displaying analysis results. **B** Qtouch home screen, where operators select the desired analysis type, e.g., cell counting (viability and density) or confluency. Main interfaces for (**C**) cell counting and (**D**) confluency experiments.

control interface. Qtouch provides comprehensive status updates throughout the analysis and allows users to save and review results at any time. The integration of real-time pump control, automated image processing, and a user-friendly interface creates a robust and adaptable platform suitable for diverse experimental conditions. Designed with resource-limited settings in mind, the system ensures accessibility while maintaining high accuracy and reproducibility. This comprehensive approach of combining a mobile app, cloud server, and bluetooth-enabled pump control represents a significant advancement in cell counting and analysis, providing researchers with a powerful tool for reliable, efficient, and reproducible experiments.

Discussion

The global cell counting market is growing significantly, with a market size of $9.8 billion USD in 2022, projected to reach $19.5 billion USD by 2032. This growth, at a compound annual growth rate of 7.1%, reflects the increasing focus on advanced research fields and the need for precision and efficiency in cell-based studies[32]. In response to these demands, numerous innovative approaches have entered the market, revolutionizing traditional methodologies. Among these, smartphone microscopy has emerged as a transformative technology, leveraging compact, cost-effective designs to democratize access to advanced imaging capabilities. Its application across diverse domains highlights its potential to bridge the gap between high-end laboratory systems and resource-limited settings, making it a pivotal tool in the evolving landscape of cell analysis[33]. Quantella directly addresses this unmet need by providing an integrated, automated, and cost-effective solution for cell viability, density, and confluency measurements. This multifunctionality, paired with smartphone compatibility and minimal hardware complexity, uniquely positions Quantella among emerging technologies in the expanding cell analysis market. In recent years,

Table 1 | Cell lines verified on Quantella

Cell	Species	Type	Growth Mode	Cell size (μm)	Why chosen
NCI-H28[53]	Human	Mesothelioma	Adherent	25	Large size and spherical morphology
SW480[54]	Human	Colon Adenocarcinoma	Adherent	~17	Low contrast cells
CHO DG44[55]	Chinese Hamster	Ovary	Suspension	12–14	Large size and spherical morphology
HEK293[56]	Human	Embryonic Kidney	Suspension	14–16	Large size and spherical morphology
Huh-7[57]	Human	Hepatocellular Carcinoma	Adherent	~22	Low contrast cells
Jurkat[58]	Human	Leukemia cells	Suspension	~10.5	Small cell size
A2780cis[59]	Human	Ovarian carcinoma	Adherent	~20	Low contrast cells
Mahlavu[60]	Human	Hepatocellular Carcinoma	Adherent	20–30	Large spherical morphology
SK-BR-3[61]	Human	Breast cancer	Adherent	15–17	Low contrast cells and heterogeneous morphologies
MCF-7[62]	Human	Breast cancer	Adherent	~20	Grow in rafts
SNU-449[63]	Human	Hepatocellular Carcinoma	Adherent	15–30	Large spherical morphology
RBC[64]	Rabbit	Red blood cells	Primary	~6.8	Small spherical morphology

Quantella can count cells with a round shape after trypsinization.

smartphone-based microscopy has gained significant attention for its application in cell counting, with numerous advancements in the field. For instance, De Haan et al. developed a smartphone-based microscope integrated with deep learning to count sickle cells, achieving 98% accuracy and analyzing 9630 RBCs per patient in under 7 s, with image quality comparable to laboratory-grade microscopes[34]. Similarly, Zhu et al. introduced a comprehensive platform capable of measuring RBC and white blood cell (WBC) densities and hemoglobin concentration, demonstrating high correlation coefficients, e.g., ~0.98, with standard hematology analyzers using only ~10 μL of blood[35]. Rabha et al. showcased a dual-function smartphone-based microscopy system for brightfield and fluorescence imaging, achieving a resolution of 1.21 μm and a large FOV, validated with microbeads and blood samples[36]. Zeng et al. developed a cost-effective cell counter using a PDMS microfluidic chip and a single-ball lens, offering high accuracy for somatic cell analysis with an estimated cost of ~$20, making it accessible for resource-limited settings[37]. Kang et al. introduced a brightfield smartphone-based counter that utilizes trypan blue staining to measure cell viability and concentration with resolution comparable to flow cytometry, maintaining low error rates across a wide range of cell densities and viability conditions[38].

In this respect, Quantella provides optically and digitally enhanced high-resolution cell imaging, enabling precise identification and quantification of cell viability, density, and confluency. Leveraging its robust imaging capabilities, Quantella supports a diverse range of cell types, including commonly utilized cell lines and primary cells such as RBCs, as outlined in Table 1. This versatility aligns Quantella with the performance of commercial devices while offering a substantially lower cost, positioning it as a practical solution for both academic and clinical applications. By combining advanced image processing with smartphone-based technology, Quantella bridges the gap between high-end laboratory systems and more accessible, cost-effective platforms, ensuring that precision cell analysis is available even in resource-limited settings. Its compatibility with various cell types and validation against commercial standards underscore its potential as a reliable, scalable tool for routine and high-throughput cell analysis. Unlike many systems that specialize in only one aspect of cell analysis or require separate instrumentation for each function, Quantella delivers an all-in-one platform capable of high-resolution imaging, accurate quantification, and robust segmentation e.g., all operated through an intuitive smartphone interface. This unified approach significantly reduces cost, training requirements, and operational complexity.

Table 2 shows a comparison of commercially available cell counting platforms, including Countess 3, LUNA-II, or Vi-Cell BLU, which utilize advanced technologies such as image processing and machine learning. These technologies offer a range of features, including diverse counting ranges, chamber designs, and performance metrics, to cater to various research applications, while providing efficient and reliable solutions, making them valuable tools for laboratories with specific analytical requirements.

In addition to cell viability-density technologies, there are also commercially available solutions that leverage advanced imaging systems integrated with image-processing algorithms or artificial intelligence (AI)-driven approaches for confluency analysis. For example, the CELENA® X High Content Imaging System (Logos Biosystems) leverages image-processing algorithms to integrate live cell imaging with confluency analysis, delivering a robust and precise solution for effective cell culture monitoring[39]. The Axion BioSystems Confluency Module, an image-processing-based software integrated into the Omni and Lux platforms, provides automated, label-free measurement of cell confluency[40]. Another example is the CKX-CCSW Confluency Checker Software (Olympus), specifically designed for use with the CKX53 inverted microscope, employs image-processing techniques and is compatible with various culture vessels, ensuring efficient and versatile confluency analysis[41]. The ZEISS Labscope utilizes an AI-driven technology to deliver accurate confluency measurements, which operates independently of cell shape, size, or type for monitoring cell populations effectively[42]. The Incucyte® Base Analysis Software (Sartorius) is a live-cell imaging and analysis tool that utilizes an AI-driven cell segmentation algorithm, enabling accurate analysis across diverse cell types and morphologies with minimal user input[43]. Mateo TL Digital Microscope (Leica Microsystems) integrates AI-powered workflows to enable automated confluency measurements and transfection efficiency assessments[44]. The EVOS™ M3000 Imaging System (Thermo Fisher Scientific) is a digital inverted microscope equipped with AI-based algorithms for precise analysis of cell confluency, delivering high-quality results for routine and advanced applications[45].

In light of these commercial approaches, Quantella demonstrates significant advancements in cell analysis by integrating innovative methodologies that combine viability, density, and confluency measurements into a single platform. Unlike the traditional methods that require sophisticated optical setups or specific imaging conditions, Quantella leverages a robust image-processing algorithm that normalizes illumination and dynamically adapts to varying experimental setups. This capability ensures consistent performance across a wide range of conditions, even in resource-limited environments[46–48]. Independence from user-defined parameters is another important aspect of Quantella's design. The system employs image-processing techniques, e.g., adaptive thresholding, variance filtering, and gradient magnitude analysis, that are not dependent on cell morphology. This feature allows Quantella to accurately analyze diverse cell types, including suspension and adherent cells, while AI-based systems often

Table 2 | Comparison of Quantella with commercial cell counting platforms

Device Name	Method	Density Range (cells/mL)	Counting Area (mm^2)	Counting Chamber	Variability
Quantella	Image Processing	2×10^4–1×10^7	13.44	Reusable or Disposable Slides	Mean Error <6.37% Precision, Recall, f1 Score >92
Countess 3 Automated Cell Counter[65,66]	Machine Learning	1×10^4–1×10^8	3.82	Reusable or Disposable Slides	The count-to-count specification is <10%.
Countess II Automated Cell Counter[67,68]	Image Processing	1×10^4–1×10^7	3.48	Disposable Slides	The count-to-count variability with the Countess II instruments is less than 10%.
TC-20 Automted Cell Counter[69]	Image Processing	5×10^4–1×10^7	4	Disposable Slides	NA
LUNA-III[70,71]	Machine Learning	5×10^4–1×10^7	5	Reusable or Disposable Slides	Coefficient of variance (CV) values consistently below 2%.
Vi-Cell BLU[72]	Image Processing	5×10^4–1.5×10^7	1	Integrated Flow Cell	Counting accuracy ±10%, Counting repeatability ±5%
Cellometer Auto T4[73]	Image Processing	1×10^5–1×10^7	4	Disposable Slides	Coefficient of Variation under 5%
CellDrop[74,75]	NA	7×10^2–2.5×10^7	1	Single-Use Plastic Slides or Reusable Slides	NA
Cedex HiRes Analyzer[76]	Image Processing	5×10^4–1×10^7	NA	Integrated Flow Cell	NA

require extensive training on large datasets and struggle with unseen cell morphologies, leading to reduced accuracy[49,50]. Quantella processes large sample sizes, analyzing over 10,000 cells per test, which reduces statistical variation, especially in heterogeneous cell populations. This approach achieves deviations of less than 5% with respect to flow cytometry, highlighting Quantella's precision and reliability[38,51]. For cell counting, Quantella incorporates an advanced image-processing algorithm that enhances raw data through multi-exposure fusion and gamma correction, optimizing images for segmentation. This approach employs weight maps, such as Laplacian Contrast, Well-Exposedness, and Brightness, to address challenges like faint cell boundaries, uneven illumination, and varying intensities. Our approach ensures robust segmentation across different cell morphologies, densities, and experimental conditions. Advanced edge detection methods, including variance and entropy filtering combined with double-thresholding, refine the accuracy of cell boundary detection. Morphological operations like hole filling and edge smoothing further enhance the integrity of detected cell structures. This sophisticated segmentation pipeline not only ensures accurate confluency measurements but also improves reproducibility across experiments[38,47]. Crucially, Quantella achieves these results without reliance on deep learning models or cell-specific calibration, enabling generalizability across diverse experimental conditions and cell morphologies. This adaptability eliminates the limitations commonly seen in AI-driven platforms, which often struggle with unseen or heterogeneous data.

Quantella's ability to integrate confluency, viability, and density measurements into a single platform offers significant operational and cost advantages. Unlike commercial systems that often require separate modules or software for different analyses, Quantella consolidates all functionalities into one system. This integration reduces operational complexity, enhances usability, and allows researchers to switch between different experiments without additional equipment or configurations. The platform's low-cost design, including a smartphone-based imaging system and rinsable flow cell, further enhances its accessibility and versatility. By supporting both single-use and multi-use modes, Quantella provides a practical solution for diverse research needs, including resource-limited environments. The validated cleaning protocol ensures that performance is maintained across repeated analyses, extending the utility and reliability[52].

While Quantella has demonstrated robust performance in cell analysis, several strategies could further enhance its capabilities. These improvements aim to increase accuracy, expand functionality, and support a broader range of applications. Using smartphones with higher-resolution cameras and advanced imaging sensors could improve image quality, enabling more precise cell segmentation and detection. Replacing the current LED with a more uniform illumination source would reduce image artifacts and enhance overall system accuracy by ensuring consistent lighting across the entire FOV. In addition, incorporating a low-cost motorized linear stage for automated focusing could further simplify user operation and enhance reproducibility across experiments. Autofocus integration would allow Quantella to dynamically adapt to varying sample thicknesses and ensure optimal imaging conditions without manual intervention, thereby increasing reliability in high-throughput or decentralized diagnostic workflows. Replacing smartphone with a Raspberry Pi module could enable local image processing, reducing reliance on cloud-based servers and enhancing real-time data analysis. This upgrade would support offline operation, making Quantella suitable for use in remote or resource-limited environments. Integrating a Raspberry Pi camera alongside this module would expand the system's FOV, allowing for the capture of larger sample areas. This improvement would support higher-throughput cell counting, minimize statistical variation, and increase platform's scalability for various experimental setups. Finally, expanding validation experiments to include a broader range of cell types would enhance Quantella's versatility and generalizability. This approach would ensure compatibility with diverse biological samples, making the platform suitable for a wider range of research and clinical applications.

Methods

Hardware design and manufacturing

For hardware control and data acquisition/management, a 2019 Oppo Reno 10× Zoom model was used. SOLIDWORKS 2019 (version SP4.0) was utilized for the design and assembly of 3D components. For 3D printing, a Polylactic Acid-based 3D printer (MakerBot Replicator +) was used, with designs optimized using MakerBot Print (version 4.10.1.2056), and a stereolithography (SLA) resin printer (Formlabs Form3) was used, with models prepared using PreForm software (version 3.43.1). Epilog Mini 18 laser cutter was utilized for laser cutting tasks. The files were prepared and

optimized for cutting using CorelDRAW X7 (version 17.1.0.572). Printed Circuit Board (PCB) prototyping was performed using Proteus 8 Professional (version 8.15 SP1) for schematic design, simulation, and PCB layout. FR4 copper-clad boards with 35 µm copper layers served as the base material for PCB fabrication. Gerber files generated in Proteus were converted into G-code using FlatCAM (version 8.991 Beta). StepCraft M500 CNC machine, controlled by the M.500 application, was employed to mill the PCBs.

Suspension and adherent cell culture

This study did not involve any human research participants, human tissue, or human data. All cell lines used in the experiments were commercially available and obtained from certified suppliers. Therefore, approval from an institutional review board or ethics committee and informed consent were not required.

The performance of Quantella was evaluated across a wide range of cell lines. HEK 293, CHO DG44, and Jurkat cells are suspension cell lines, and thus do not require detachment. These cultures were maintained at 37 °C, 8% CO_2, and 90% humidity, and shaking at 130 rpm. All other cell lines, including HuH-7, SW-480, SNU-449, SK-BR-3, MCF-7, Mahlavu, NCI-H28, A2780cis, and L929, are adherent cell lines and were detached from the culture surface via trypsinization (Sigma-Aldrich®) upon reaching 80% confluency. Detached cells were then suspended in fresh medium, with PBS (Sigma-Aldrich®) used for rinsing during the suspension preparation. The cells were maintained at 37 °C, 5% CO_2, and 95% humidity.

Human Embryonic Kidney (HEK 293) cell line was cultured in a serum-free medium comprising CD FortiCHO medium (Gibco™) supplemented with 6 mM L-glutamine (Gibco™). Chinese Hamster Ovary (CHO DG44) cell line was cultured in a serum-free medium composed of CD DG44 medium (Gibco™) supplemented with 8 mM L-glutamine (Gibco™) and 18 mL/L Pluronic F-68 (10%, Gibco™). Hepatocellular Carcinoma cells were cultured in high-glucose DMEM supplemented with 10% FBS (Sigma-Aldrich®), 100 µg/mL streptomycin (Sigma-Aldrich®), and 100 units/mL penicillin (Sigma-Aldrich®). Human Colon Adenocarcinoma SW480 (Primary Tumor) cells, derived from a primary pre-metastatic colorectal tumor, were cultured in complete DMEM (cDMEM) supplemented with 100 µg/mL streptomycin (Gibco™), 100 units/mL penicillin (Gibco™), and 10% FBS (Sigma-Aldrich®). Hepatocellular Carcinoma (SNU-449) cells were maintained in RPMI medium supplemented with 1% nonessential amino acids solution (Gibco™), 1% sodium pyruvate (Gibco™), 10% heat-inactivated FBS (Gibco™), 100 units/mL penicillin (Gibco™), and 100 µg/mL streptomycin (Gibco™). Human Breast Cancer (SK-BR-3) cells, a human breast cancer cell line overexpressing HER2 (Human Epidermal Growth Factor Receptor 2), were cultured in DMEM/F12 medium (Gibco™), supplemented with 10% FBS (Sigma-Aldrich®) and 1% penicillin-streptomycin-amphotericin B (Gibco™). Breast Cancer (MCF-7) cells were cultured in RPMI 1640 medium (Sigma-Aldrich®), supplemented with 10% fetal bovine serum (FBS, Sigma-Aldrich®), 100 units/mL penicillin (Sigma-Aldrich®), and 100 µg/mL streptomycin (Sigma-Aldrich®). Human Hepatocellular Carcinoma (Mahlavu) cells were cultured in glucose-enriched DMEM (Gibco™), supplemented with 10% fetal bovine serum (FBS, Sigma-Aldrich®), 100 units/mL penicillin (Gibco™), 100 µg/mL streptomycin (Gibco™), and 2 mM L-glutamine (Gibco™). Jurkat cells, an immortalized cell line derived from human T-cell leukemia, were cultured in RPMI-1640 medium (Sigma-Aldrich®), supplemented with 10% fetal bovine serum (FBS, Sigma-Aldrich®), 100 units/mL penicillin (Sigma-Aldrich®), and 100 µg/mL streptomycin (Sigma-Aldrich®). Human Mesothelioma (NCI-H28) cells were cultured in RPMI-1640 medium supplemented with 10% FBS (Sigma-Aldrich®), 100 units/mL penicillin (Gibco™), and 100 µg/mL streptomycin (Gibco™). Cisplatin-Resistant Ovarian (A2780cis) cells were grown in RPMI medium containing 10% FBS (Sigma-Aldrich®), 2 mM L-glutamine (Gibco™), 100 units/mL penicillin (Gibco™), and 100 µg/mL streptomycin (Gibco™). Mouse Fibroblast (L929) cells were cultured in high-glucose DMEM (4.5 g/L, Gibco™) supplemented with 10% fetal bovine serum (FBS, Sigma-Aldrich®), 100 units/mL penicillin (Sigma-Aldrich®), and 100 µg/mL streptomycin (Sigma-Aldrich®). To obtain 72 h post-fertilization (hpf) Zebrafish larvae, adult male and female zebrafish were paired at a 1:1 ratio and housed overnight with a spawning grid in place. After spawning, adult fish were removed, and the collected eggs were transferred to a petri dish containing E3 medium for incubation at 28.5 °C. The medium was refreshed daily to maintain optimal conditions, and larvae exhibiting active movement and normal development were selected for further use.

Calibration study with Quantella, manual counting, and flow cytometry

For the calibration study involving Quantella, manual counting and flow cytometry, various cell densities were prepared. For HEK293 cells, the tested densities were, e.g., 20×10^3, 40×10^3, 70×10^3, 150×10^3, 400×10^3, 750×10^3, 1×10^6, 3.4×10^6, 10×10^6, and 19×10^6 cells/mL. For CHO DG44 cells, the following densities were tested, e.g., 20×10^3, 120×10^3, 250×10^3, 300×10^3, 480×10^3, 775×10^3, 2×10^6, 4.5×10^6, 10×10^6, and 18×10^6 cells/mL. For manual cell counting with the Thoma chamber and Quantella, each cell solution was mixed with trypan blue Solution (0.4%, Gibco™) at a 1:1 ratio. After each set of measurements, the chamber was cleaned with 80% ethanol. For Quantella, the flow cell was flushed with an EDTA-PEG-containing medium to eliminate cell adherence, and between each test, it was washed three times with PBS and distilled water. For flow cytometry measurements, 5 µL of PI was added to each solution, and the samples were vortexed. Measurements were conducted with a NovoCyte Advanteon flow cytometer (Agilent Technologies, Inc.).

Confluency analyses with MCF-7 cells

MCF-7 cells, seeded at a density of 1×10^4 cells/mL under RPMI-1640 medium, were incubated for 48 h in a commercial incubator set at 37 °C with a humidified atmosphere containing 5% CO_2. Following the incubation, cell confluency and morphology were assessed with Quantella.

Paclitaxel (PTX) sensitivity of MCF-7 cells

MCF-7 cells were initially seeded at a density of 4×10^4 cells/mL. The experiment includes two groups, e.g., control and PTX-treated. PTX was purchased from Selleck Chemicals, Houston, TX, USA. The PTX stock solution was prepared by dissolving in dimethyl sulfoxide (DMSO, Thermo Scientific) at a concentration of 50 mM, then diluted with culture medium to achieve a final concentration of 1000 nM for treatment. Confluency images of control and PTX-treated groups were captured after 24 h (incubated in a commercial incubator), using Quantella to visualize the morphological changes induced by PTX treatment.

Effects of doxorubicin hydrochloride (DOX) on Jurkat cells

DOX was obtained from Selleck Chemicals and dissolved in DMSO to create a 2 mM stock solution. The stock was diluted with culture medium to achieve a range of final concentrations for treatment. Jurkat cells were initially seeded at a density of 4×10^4 cells/mL. Cells were treated with various concentrations of DOX, e.g., 0, 1, 10, 50, 125, and 500 nM, incubated for 24, 48, and 72 h in a commercial incubator to evaluate both time- and dose-dependent drug effects. At each time point, cell viability was assessed using Quantella.

Serum starvation in Mahlavu cells

Mahlavu cells were seeded at a density of 1.3×10^4 cells/mL and incubated for 24 h in complete medium containing 10% FBS. Following the initial incubation, the medium was replaced to establish two groups, e.g., the control group receiving fresh medium with 10% FBS, and the experimental group receiving FBS-free medium. After an additional 48 h incubation in a commercial incubator, the cells were observed via Quantella and MTT to assess the cellular response to serum deprivation. In the MTT assay, MTT [3-(4,5-dimethylthiazol-2-yl)-2,5-diphenyltetrazolium bromide] (Thermo Fisher Scientific™) solution was prepared in 1× PBS (Gibco™). A volume of 10 µL of the MTT solution (5 mg/mL) was added to each well, and the plate was incubated at 37 °C for 4 h to facilitate the formation of formazan crystals. Following incubation, the medium was discarded, and 100 µL of

DMSO (Thermo Fisher Scientific™) was added to each well. The plate was placed on an orbital shaker (Thermo Fisher Scientific™) for 25 min to ensure complete dissolution of the formazan crystals. MTT assay was conducted with absorbance measured at 590 nm using a Multiskan FC Microplate Photometer (Thermo Scientific).

Red blood cells (RBC) counting

RBCs were obtained from the blood sample collected from a 45-week-old New Zealand rabbit provided by the IBG-Vivarium Rodent Unit. All experimental procedures were approved by the Animal Experimentation Local Ethics Committee of Izmir Biomedicine and Genome Center, and adhered to the European Community guidelines (86/609/EEC) for the protection of animals used in scientific research. Prior to blood collection, the animal was anesthetized via intramuscular administration of ketamine (35 mg/kg) and xylazine (5 mg/kg), followed by cardiac puncture for blood withdrawal. To prevent coagulation, blood samples were collected in K2-EDTA anticoagulant tubesImmediately after blood collection, euthanasia was performed by intravenous administration of 0.3 ml/animal of T61 euthanasia solution. Following appropriate restraint of the rabbits, the lateral surface of the leg was shaved and disinfected. Blood was then collected from the saphenous vein using a 26G cannula. To prevent coagulation, the blood was transferred into K2-EDTA tubes. Following collection, a full blood count was conducted using a hematology analyzer. The blood samples were then diluted 1:5 with PBS and centrifuged at $500 \times g$ for 15 min. After centrifugation, the supernatant was discarded, and the pellet was resuspended in PBS at a 1:10 ratio, followed by another centrifugation at $500 \times g$ for 15 min. The washing process was repeated until pure RBCs were obtained. Once purified, the pellet was resuspended in PBS for counting. Animal housing, husbandry, and welfare monitoring followed institutional standard operating procedures, with efforts made to minimize suffering.

Data availability

The code used to generate the findings is available in the Zenodo repository (https://doi.org/10.5281/zenodo.14905633). The repository includes demo files for (i) Image enhancement algorithm for robust segmentation, (ii) cell counting algorithm, (iii) cluster segmentation algorithm, (iv) confluency analysis algorithm, and (v) performance evaluation of cell counting for RBCs. The demo files contain README documentation, input images (used in the manuscript), and executable files of the algorithms. The repository also provides MATLAB codes with all necessary functions, including a cell counting example of CHO DG44 cells at 20×10^3 cells/mL and a confluency analysis example of MCF-7 cells with 33.7% confluency. The provided MATLAB scripts can be executed without requiring a MATLAB installation, as they are compiled for standalone execution (https://doi.org/10.5281/zenodo.14905633).

Received: 27 March 2025; Accepted: 5 June 2025;
Published online: 22 October 2025

References

1. Vembadi, A., Menachery, A. & Qasaimeh, M. A. Cell cytometry: review and perspective on biotechnological advances. *Front. Bioeng. Biotechnol*. **7**, 147 (2019).
2. Shroff, H., Testa, I., Jug, F. & Manley, S. Live-cell imaging powered by computation. *Nat. Rev. Mol. Cell Biol.* **25**, 443–463 (2024).
3. Phelan, M. C. Basic techniques in mammalian cell tissue culture. *Curr. Protoc. Cell Biol*. **36**, 1.1.1–1.1.22 (2007).
4. Freshney, R. I. Basic principles of cell culture. In *Culture of Cells for Tissue Engineering* 1–22. https://doi.org/10.1002/0471741817.ch1 (Wiley, 2005).
5. Honrado, C., Bisegna, P., Swami, N. S. & Caselli, F. Single-cell microfluidic impedance cytometry: from raw signals to cell phenotypes using data analytics. *Lab Chip* **21**, 22–54 (2021).
6. Han, Y., Gu, Y., Zhang, A. C. & Lo, Y.-H. Review: imaging technologies for flow cytometry. *Lab Chip* **16**, 4639–4647 (2016).
7. Stringer, C., Wang, T., Michaelos, M. & Pachitariu, M. Cellpose: a generalist algorithm for cellular segmentation. *Nat. Methods* **18**, 100–106 (2021).
8. Greenwald, N. F. et al. Whole-cell segmentation of tissue images with human-level performance using large-scale data annotation and deep learning. *Nat. Biotechnol.* **40**, 555–565 (2022).
9. Falk, T. et al. U-Net: deep learning for cell counting, detection, and morphometry. *Nat. Methods* **16**, 67–70 (2019).
10. Yu, Y. et al. Detection of cells by flow cytometry: counting, imaging, and cell classification. *J. Innov. Opt. Health Sci*. **16**, 2330005 (2023).
11. Tang, T. et al. A review on intelligent impedance cytometry systems: development, applications and advances. *Anal. Chim. Acta* **1269**, 341424 (2023).
12. Schaaf, T. M., Peterson, K. C., Grant, B. D., Thomas, D. D. & Gillispie, G. D. Spectral unmixing plate reader: high-throughput, high-precision FRET assays in living cells. *SLAS Discov.* **22**, 250–261 (2017).
13. Tennant, J. R. Evaluation of the trypan blue technique for determination of cell viability. *Transplantation* **2**, 685–694 (1964).
14. Topman, G., Sharabani-Yosef, O. & Gefen, A. A method for quick, low-cost automated confluency measurements. *Microsc. Microanal.* **17**, 915–922 (2011).
15. Duran, I. et al. Detection of senescence using machine learning algorithms based on nuclear features. *Nat. Commun.* **15**, 1041 (2024).
16. Nguyen, T. H. et al. Halo-free phase contrast microscopy. *Sci. Rep.* **7**, 44034 (2017).
17. Datta, R., Heaster, T. M., Sharick, J. T., Gillette, A. A. & Skala, M. C. Fluorescence lifetime imaging microscopy: fundamentals and advances in instrumentation, analysis, and applications. *J. Biomed. Opt.* **25**, 1 (2020).
18. Jain, S. et al. The complete automation of cell culture: improvements for high-throughput and high-content screening. *SLAS Discov.* **16**, 932–939 (2011).
19. Mertens, T., Kautz, J. & Van Reeth, F. Exposure fusion: a simple and practical alternative to high dynamic range photography. *Comput. Graph. Forum* **28**, 161–171 (2009).
20. Karakaya D., Ulucan, O. & Turkan, M. Pas-Mef: multi-exposure image fusion based on principal component analysis, adaptive well-exposedness and saliency map. In: *Proc. IEEE International Conference on Acoustics, Speech and Signal Processing (ICASSP 2022)* 2345–2349. https://doi.org/10.1109/ICASSP43922.2022.9746779 (IEEE, 2022).
21. Kim, Y., Ma, J., Lim, S. Y., Song, J. Y. & Yun, T. S. Determination of shape parameters of sands: a deep learning approach. *Acta Geotech.* **17**, 1521–1531 (2022).
22. Petenkaya, E. D., Lacin, O. B., Kara, O. F. & Turkan, M. Underwater image dehazing via red-channel recovery. In: *Proc. 31st European Signal Processing Conference (EUSIPCO)* 531–535. https://doi.org/10.23919/EUSIPCO58844.2023.10289765 (IEEE, 2023).
23. Sarkar, S. et al. Evaluating the quality of a cell counting measurement process via a dilution series experimental design. *Cytotherapy* **19**, 1509–1521 (2017).
24. Centonze Frohlich, V. Phase contrast and differential interference contrast (DIC) microscopy. *J. Vis. Exp*. **17**, 844. https://doi.org/10.3791/844 (2008).
25. Yang, J., Zhu, G. & Shi, Y.-Q. Analyzing the effect of JPEG compression on local variance of image intensity. *IEEE Trans. Image Process.* **25**, 2647–2656 (2016).
26. Li, X., Liu, M. & Ling, Q. Pixel-wise gamma correction mapping for low-light image enhancement. *IEEE Trans. Circuits Syst. Video Technol.* **34**, 681–694 (2024).
27. Moreno, G. et al. A new focus detection criterion in holograms of planktonic organisms. *Pattern Recognit. Lett.* **138**, 497–506 (2020).
28. Sonka, M., Hlavac, V. & Boyle, R. *Image Processing, Analysis and Machine Vision*. https://doi.org/10.1007/978-1-4899-3216-7 (Springer, 1993).

29. Bhattacharyya, J. et al. A paclitaxel-loaded recombinant polypeptide nanoparticle outperforms Abraxane in multiple murine cancer models. *Nat. Commun.* **6**, 7939 (2015).
30. Linders, A. N. et al. A review of the pathophysiological mechanisms of doxorubicin-induced cardiotoxicity and aging. *NPJ Aging* **10**, 9 (2024).
31. Cetin, A. E., Topkaya, S. N., Yalcin-Ozuysal, O. & Khademhosseini, A. Refractive index sensing for measuring single cell growth. *ACS Nano* **15** https://doi.org/10.1021/acsnano.1c04031 (2021).
32. Richards, C., Sarkar, S., Kandell, J., Snyder, R. & Lakshmipathy, U. Assessing the suitability of cell counting methods during different stages of a cell processing workflow using an ISO 20391-2 guided study design and analysis. *Front. Bioeng. Biotechnol*. **11**, 1223227 (2023).
33. Wang, B. et al. Smartphone-based platforms implementing microfluidic detection with image-based artificial intelligence. *Nat. Commun.* **14**, 1341 (2023).
34. de Haan, K. et al. Automated screening of sickle cells using a smartphone-based microscope and deep learning. *NPJ Digit. Med.* **3**, 76 (2020).
35. Zhu, H. et al. Cost-effective and rapid blood analysis on a cell-phone. *Lab Chip* **13**, 1282 (2013).
36. Rabha, D. et al. An affordable, handheld multimodal microscopic system with onboard cell morphology and counting features on a mobile device. *Analyst* **147**, 2859–2869 (2022).
37. Zeng, Y. et al. A low cost and portable smartphone microscopic device for cell counting. *Sens. Actuators A* **274**, 57–63 (2018).
38. Kang, W. et al. On-site cell concentration and viability detections using smartphone-based field-portable cell counter. *Anal. Chim. Acta* **1077**, 216–224 (2019).
39. CELENA® X High Content Imaging System https://logosbio.com/celena-x/ (2024).
40. Axion BioSystems Confluency Module https://www.axionbiosystems.com/products/imaging/imaging-software/confluency-module (2024).
41. CKX-CCSW Confluency Checker Software https://www.olympus-lifescience.com/en/cell_culture_solution/ckx-ccsw/ (2024).
42. ZEISS Labscope https://www.zeiss.com/microscopy/en/products/software/zeiss-labscope/zeiss-labscope-lab.html#highlights (2024).
43. Incucyte® Software Modules for Powerful Phenotypic Cellular Analysis https://www.sartorius.com/en/products/live-cell-imaging-analysis/live-cell-analysis-software (2024).
44. Mateo Digital Microscopes https://www.leica-microsystems.com/products/light-microscopes/p/mateo/specification/ (2024).
45. EVOS M3000 Imaging System https://www.thermofisher.com/tr/en/home/life-science/cell-analysis/cellular-imaging/evos-cell-imaging-systems/models/evos-m3000.html (2024).
46. Talebian, S. & Javanmard, M. Compact and automated particle counting platform using smartphone-microscopy. *Talanta* **228**, 122244 (2021).
47. Chen, Y.-W. & Chiang, P.-J. An automated approach for hemocytometer cell counting based on image-processing method. *Measurement* **234**, 114894 (2024).
48. Riccio, D., Brancati, N., Frucci, M. & Gragnaniello, D. A new unsupervised approach for segmenting and counting cells in high-throughput microscopy image sets. *IEEE J. Biomed. Heal. Inform.* **23**, 437–448 (2019).
49. Bai, H., Wang, X., Guan, Y., Gao, Q. & Han, Z. Blood cell counting based on U-Net++ and YOLOv5. *Optoelectron. Lett.* **19**, 370–376 (2023).
50. Sun, Y. & Guo, X. Research on three-dimensional counting algorithm of high-precision suspended cells based on deep learning. *J. Electron. Imaging* **31**, 043018 (2022).
51. Ilyas, S., Sher, M., Du, E. & Asghar, W. Smartphone-based sickle cell disease detection and monitoring for point-of-care settings. *Biosens. Bioelectron.* **165**, 112417 (2020).
52. Chadha, G. K., Srivastava, A., Singh, A., Gupta, R. & Singla, D. An automated method for counting red blood cells using image processing. *Procedia Comput. Sci.* **167**, 769–778 (2020).
53. Mutsaers, S. E. & Herrick, S. E. Mesothelial cells. In *Encyclopedia of Respiratory Medicine* 47–52. https://doi.org/10.1016/B0-12-370879-6/00246-5 (Elsevier, 2006).
54. Gala de Pablo, J. et al. Biochemical fingerprint of colorectal cancer cell lines using label-free live single-cell Raman spectroscopy. *J. Raman Spectrosc.* **49**, 1323–1332 (2018).
55. Pan, X., Dalm, C., Wijffels, R. H. & Martens, D. E. Metabolic characterization of a CHO cell size increase phase in fed-batch cultures. *Appl. Microbiol. Biotechnol.* **101**, 8101–8113 (2017).
56. Seidel, S., Maschke, R. W., Mozaffari, F., Eibl-Schindler, R. & Eibl, D. Improvement of HEK293 cell growth by adapting hydrodynamic stress and predicting cell aggregate size distribution. *Bioengineering* **10**, 478 (2023).
57. Berger, E., Vega, N., Weiss-Gayet, M. & Géloën, A. Gene network analysis of glucose-linked signaling pathways and their role in human hepatocellular carcinoma cell growth and survival in HuH7 and HepG2 cell lines. *Biomed. Res. Int.* **2015**, 1–19 (2015).
58. Ferguson, C. A., Hwang, J. C. M., Zhang, Y. & Cheng, X. Single-cell classification based on population nucleus size combining microwave impedance spectroscopy and machine learning. *Sensors* **23**, 1001 (2023).
59. Cerda-Troncoso, C. et al. Chemo-small extracellular vesicles released in cisplatin-resistance ovarian cancer cells are regulated by the lysosomal function. *J. Extracell. Biol*. **3**, e157 (2024).
60. Kurden-Pekmezci, A. et al. MALT1 paracaspase is overexpressed in hepatocellular carcinoma and promotes cancer cell survival and growth. *Life Sci.* **323**, 121690 (2023).
61. Mendelaar, P. A. J. et al. Defining the dimensions of circulating tumor cells in a large series of breast, prostate, colon, and bladder cancer patients. *Mol. Oncol.* **15**, 116–125 (2021).
62. Moon, H.-S. et al. Continual collection and re-separation of circulating tumor cells from blood using multi-stage multi-orifice flow fractionation. *Biomicrofluidics* **7**, 014105 (2013).
63. Leroy, K. et al. Expression and functionality of connexin-based channels in human liver cancer cell lines. *Int. J. Mol. Sci.* **22**, 12187 (2021).
64. Melillo, A. Rabbit clinical pathology. *J. Exot. Pet. Med.* **16**, 135–145 (2007).
65. Countess 3 Automated Cell Counter. https://www.thermofisher.com/tr/en/home/life-science/cell-analysis/cell-analysis-instruments/automated-cell-counters/models/countess-3.html (2024).
66. Countess 3 Automated Cell Counters. https://assets.fishersci.com/TFS-Assets/BID/brochures/cell-counter-that-thinks-like-cell-biologist-countess-3-brochure.pdf?_ga=2.147342327.1181962328.1729168352-614917994.1729168352 (2023).
67. Countess II Automated Cell Counters https://assets.thermofisher.com/TFS-Assets/LSG/brochures/countess-II-automated-cell-counters-brochure.pdf (2017).
68. Comparison of cell counting using Countess II Automated Cell Counters vs. hemocytometers https://assets.thermofisher.com/TFS-Assets/LSG/Application-Notes/comparison-countess-hemocytometer-app-note.pdf (2016).
69. TC20 Automated Cell Counter https://www.bio-rad.com/webroot/web/pdf/lsr/literature/10024423.pdf (2024).
70. LUNA-III Automated Cell Counter https://logosbio.com/wp-content/uploads/LUNA-III%E2%84%A2_Automated-Cell-Counter_brochure.pdf (2024).
71. Reliable Cell Counting with Superior Reproducibility Using the LUNA-III Automated Cell Counter https://logosbio.com/wp-content/uploads/Application-Note-Reliable-Cell-Counting-with-Superior-Reproducibility-Using-the-LUNA-III%E2%84%A2.pdf (2024).

72. Specification Comparison of Vi–CELL XR and Vi–CELL BLU https://www.beckman.com.tr/resources/reading-material/application-notes/specification-comparison-vi-cell-xr-blu (2024).
73. Cellometer Auto T4 User Manual https://resources.revvity.com/pdfs/8001009%20Cellometer%20Auto%20T4%20User%20Manual%20Rev%20E.pdf (2024).
74. DeNovix CellDrop. https://denovix.com/pdf/celldrop-user-guide.pdf (2024).
75. CellDrop Automated Cell Counter. https://www.denovix.com/products/celldrop/ (2024).
76. Cedex HiRes Analyzer. https://custombiotech.roche.com/global/en/products/instruments/cedex-hires-ins-2157.html#productSpecs (2024).

Acknowledgments

A.E.C. acknowledges The Scientific and Technological Research Council of Türkiye (TÜBİTAK) (Project No. 119E308 and 121E620). M.B.A. acknowledges TÜBİTAK 2210/D National Industrial MSc/MA Scholarship Program. The authors would like to thank Izmir Biomedicine and Genome Center (IBG)—Pharma for HEK 293 and CHO DG44, IBG—Functional Cancer Genomics Lab. for Huh-7 and NCI-H28, IBG—Biobank for SW480, SNU-449 and Mahlavu, IBG—Stem Cell and Organoid Technologies Lab. for SK-BR-3, IBG—Biopharmaceutic Technologies and Bioanalysis Lab. for A2780cis, IBG—Vivarium for RBC, IBG—Development and Regeneration Lab. for Wild-type AB zebrafish larvae, Izmir Tinaztepe University—Ozturk Lab. for MCF-7 and Jurkat, Izmir Institute of Technology-Baldemir Lab. for L929 cell lines. The authors would also like to thank IBG—THORLAB for flow cytometry measurements, IBG—Vivarium for hemogram measurements, and IBG—Optic Imaging Facility for phase-contrast microscopy imaging. Figures 4–6 were created with BioRender.com.

Author contributions

M.B.A. designed the hardware system and developed the control software. M.B.A. and F.K. contributed to the system integration and imaging module optimization. M.B.A. and F.K. performed all experiments and prepared the figures. A.E.C. and M.T. supervised the project, guided the conceptual design, and contributed to manuscript revisions. A.E.C. received the funding. All authors wrote the main manuscript text. All authors reviewed and approved the final manuscript.

Competing interests

M.B.A., M.T., and A.E.C. have a pending patent application for the technology presented in this paper. The remaining authors declare no competing interests.

Additional information

Correspondence and requests for materials should be addressed to Arif E. Cetin.